Volume 54
Number 5
7 March 2025
Pages 2129–2656

Chem Soc Rev

Chemical Society Reviews

rsc.li/chem-soc-rev

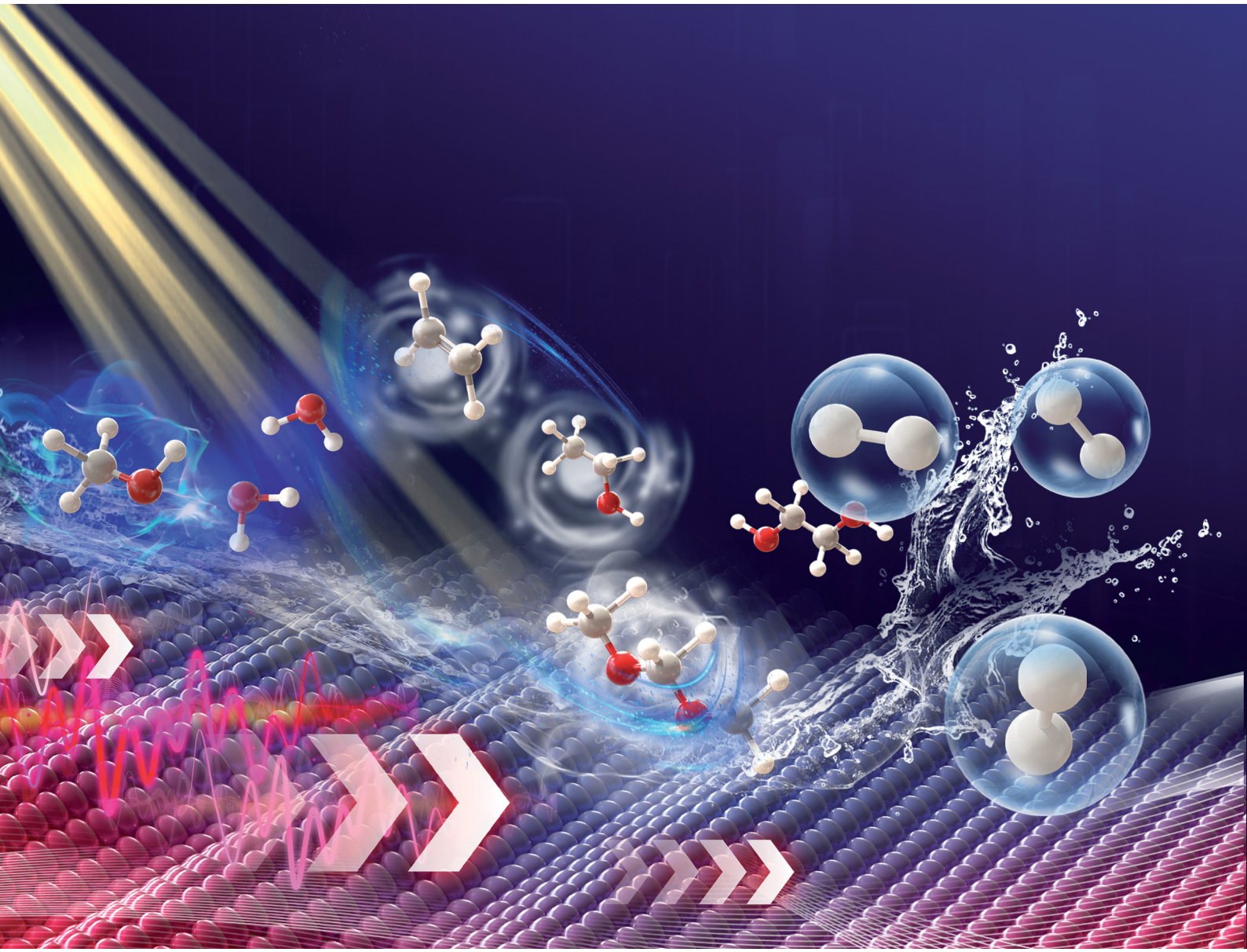

ISSN 0306-0012

ROYAL SOCIETY OF CHEMISTRY

REVIEW ARTICLE

Junwang Tang *et al.*

From photocatalysis to photon–phonon co-driven catalysis for methanol reforming to hydrogen and valuable by-products

Chem Soc Rev

REVIEW ARTICLE

View Article Online
View Journal | View Issue

Cite this: *Chem. Soc. Rev.*, 2025, **54**, 2188

From photocatalysis to photon–phonon co-driven catalysis for methanol reforming to hydrogen and valuable by-products†

Hui Wang, [ab] Eleana Harkou,[c] Achilleas Constantinou, [c] Sultan M. Al-Salemc, [d] George Manos [b] and Junwang Tang [*bef]

Hydrogen energy will play a dominant role in energy transition from fossil fuel to low carbon processes, while economical, efficient, and safe hydrogen storage and transportation technology has become one of the main bottlenecks that currently hinder the application of the hydrogen energy scale. Methanol has widely been regarded as a primary liquid H_2 storage medium due to its high hydrogen content, easy storage and transportation and relatively low toxicity. Hydrogen release from methanol using photocatalysis has thus been the focus of intense research and recent years have witnessed its fast progress and drawbacks. This review offers a comprehensive overview of methanol-based hydrogen production *via* photocatalysis, spotlighting recent developments in photocatalysts referring to thermal catalysts, including efficient semiconductors and cocatalysts, followed by the discussion of mechanistic investigation *via* advanced techniques and their disadvantages. Beyond this, particular focus has been placed on the discussion of co-driven processes involving coupling of photons (photocatalysis) with phonons (thermal catalysis) – the concept of photon–phonon co-driven catalysis – for methanol reforming and cutting-edge reactor design strategies, in order to enhance the overall process efficiency and applicability. Concluding with forward-looking insights, this review aims to provide valuable guidance for future research on hydrogen release through methanol reforming.

Received 5th September 2024

DOI: 10.1039/d4cs00551a

rsc.li/chem-soc-rev

[a] *College of Environmental Science and Engineering, Hunan University, Changsha 410082, P. R. China*
[b] *Department of Chemical Engineering, University College London (UCL), London, WC1E 7JE, UK. E-mail: jwtang@tsinghua.edu.cn*
[c] *Department of Chemical Engineering Cyprus University of Technology, 57 Corner of Athinon and Anexartisias, Limassol 3036, Cyprus*
[d] *Environment and Life Sciences Research Centre, Kuwait Institute for Scientific Research, Safat 13109, Kuwait*
[e] *Industrial Catalysis Centre, Department of Chemical Engineering, Tsinghua University, Beijing 100084, China*
[f] *Ordos Laboratory, Inner Mongolia, 017000, China*

† Electronic supplementary information (ESI) available. See DOI: https://doi.org/10.1039/d4cs00551a

Hui Wang

Dr Hui Wang is a professor at the College of Environmental Science and Engineering, Hunan University. She received her PhD in Chemical Engineering from University College London under the supervision of Prof. Junwang Tang. Her current research focuses on photo-thermal coupling for hydrogen production from biomass alcohols, as well as the high-value transformation of pollutants.

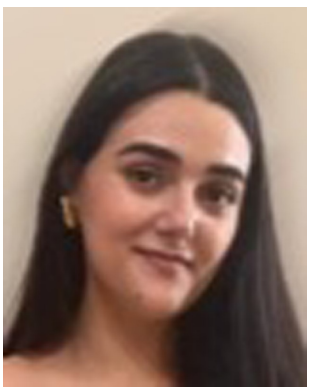

Eleana Harkou

Ms Eleana Harkou is a PhD candidate in the Cyprus University of Technology, with a background in Chemical Engineering. She is skilled in both computational fluid dynamics (CFD) simulations and process modeling, with extensive experience in the modeling, development, and scaling of chemical reactors for diverse applications and in optimising fluid flow, heat/mass transfer, and chemical processes. She specialises in the reaction engineering field with main focus on the reactor design to maximise the efficiency and performance of catalytical reaction processes.

1. Introduction

H_2 has been considered as a primary energy source to reduce our dependence on fossil fuels. It can be obtained from various renewable energy resources and can act as an energy supplier for fuel cells. However, transportation and storage of H_2 have been the biggest challenges restricting its instant commercial utilisation. On-site production of H_2 has been reported as a promising technology to meet the end-user's requirements and overcome transportation and storage challenges. Unlike organic substrates and some inert raw materials such as ethanol, lignocellulosic biomass, and glycerol, which require higher temperatures for carbon–carbon bond cleavage, methanol's molecular structure lacks carbon–carbon bonds.[1] This unique feature allows hydrogen generation from methanol to occur at relatively low temperatures, together with the high hydrogen content in methanol, making it a very practical and energy-efficient option. Kinetically, methanol's small molecular size allows it to easily adsorb and to be activated on catalyst surfaces, thereby increasing the reaction rate. Furthermore, ongoing research in the field of green methanol synthesis has demonstrated the potential of this compound as a sustainable source of hydrogen.

Traditional methanol reforming processes have predominantly relied on thermocatalysis, driving chemical reactions at relatively high temperatures. However, it often demands significant energy inputs and produces a large amount of CO_2,

Achilleas Constantinou

Dr Achilleas Konstantinou is an assistant Professor at the Cyprus University of Technology (CUT). He specializes in Chemical and Catalytic Reaction Engineering and, in particular, in designing multiphase reactors to intensify and improve their performance for industrial applications. Dr Konstantinou has made extensive use of complex Computational Fluid Dynamics (CFD) tools and successfully validated the prediction of concentrations, temperatures and velocity profiles in micro-units against experimental findings, in order to improve their design and render them suitable for industrial production. Dr Konstantinou also holds the titles of Chartered Chemical Engineer (MIChemE), Chartered Engineer (CEng) and Chartered Scientist (CSci).

Sultan M. Al-Salemc

Dr Sultan M. Al-Salem specialises in polymer degradation kinetics, a particular research interest of his. He is also interested in polymer weathering, Plastic Solid Waste (PSW) management, reactor design, downstream intensification processes, Waste Management, thermal engineering, life cycle assessment (LCA), biodegradable polymers, microplastics (MPs) and off-gas engineering. Dr Al-Salem has authored/co-authored a number of book chapters, refereed journal and conference papers. He currently holds the position of a Research Scientist at the Environment & Life Sciences Research Centre (ELSRC) of the Kuwait Institute for Scientific Research (KISR) working on various research projects and pursuing a number of major R&D works.

George Manos

Dr George Manos is an Associate Professor in Chemical Engineering at University College London (UCL). His research involves hydrocarbon reaction processes with a focus on plastic waste catalytic pyrolysis and more generally catalysis of renewable energy processes. He is also working on catalyst deactivation by coking and coke characterisation, as well as statistical mechanical modelling of adsorption on microporous materials. Dr Manos is the author of more than one hundred refereed journal papers, as well as numerous book chapters and conference papers. He is the co-editor of the book Adsorption and Phase Behaviour in Nanochannels and Nanotubes.

Junwang Tang

Prof. Junwang Tang is a Member of Academia Europaea, a Leverhulme Trust Senior Research Fellow, Fellow of RSC and Fellow of IMMM and formerly a full Professor at Chemical Engineering in University College London. He is currently a Chair Professor of Materials Chemistry and Catalysis in the Department of Chemical Engineering and Director of the Industrial Catalysis Centre at Tsinghua University. He has concentrated on photocatalysis and pioneered in photon–phonon co-driven catalysis for the activation of small molecules (e.g., H_2O, CO_2, CH_4, and N_2) as well as microwave catalytic depolymerisation of plastics. He has received many prestigious honors, including the 2022 IChemE Oil and Gas Award, the 2021 IChemE Andrew Medal, the 2021 RSC Corday-Morgan Prize, and the 2021 IChemE Innovative Product Award.

which can undermine its sustainability. In contrast, photocatalysis offers a more energy-efficient alternative by utilising light energy, typically solar, to activate catalysts for hydrogen production. This approach not only harmonises with renewable energy strategies but also operates under considerably milder conditions compared to thermocatalysis, enhances valuable by-product selectivity and reduces energy consumption. Current progress increasingly highlights the vast potential of photocatalysis, particularly when compared to thermocatalysis, as depicted in Fig. 1. Significant advancements have been made in enhancing hydrogen generation activity and valuable by-product selectivity through photocatalytic processes. The scientific community is vigorously pushing technological boundaries, engineering innovative materials, refining catalytic conditions, and unravelling complex reaction mechanisms. However, despite these advances, a comprehensive summary involving photocatalytic methanol dehydrogenation and practical reactor design referring to thermal catalysis remains notably lacking. This review aims to bridge this gap by starting with the advantages and drawbacks of thermal catalysis as a reference and then detailing photocatalytic hydrogen production from methanol. It presents a thorough examination of the latest developments, highlighting diverse photocatalysts and focusing on by-product selectivity – an aspect to some extent overlooked in prior reviews. Following that, special attention is devoted to strategically coupling photons with phonons for a catalytic process (the concept of photon–phonon co-driven catalysis), which was firstly underlined by our group recently, a combination to address individual limitations, complementary by the reactor design. Therefore, this review concludes with forward-looking insights, aiming to enhance understanding and to spur further innovation in the field of efficient photocatalytic hydrogen production and valuable by-product synthesis.

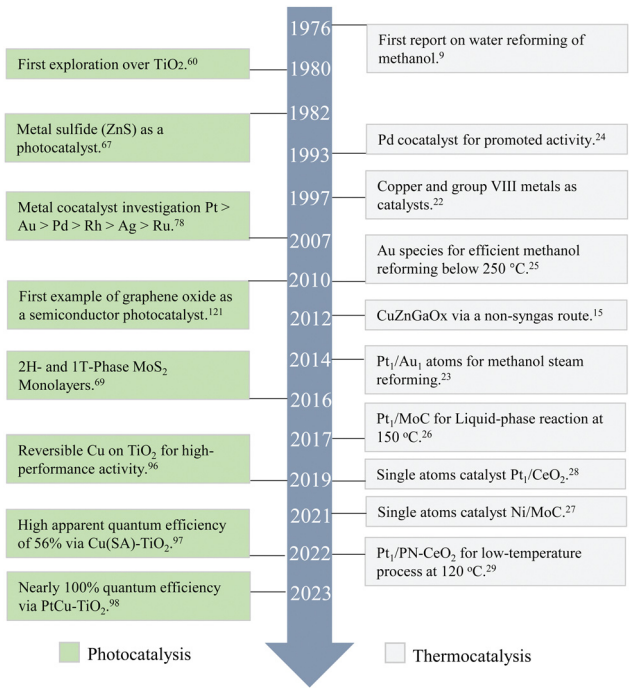

Fig. 1 The development of methanol-based hydrogen production *via* photocatalysis and thermocatalysis.

2. Thermocatalytic methanol-based hydrogen production

The generation of hydrogen from methanol–water reforming under thermal conditions is a conventional method where catalysts with high activities were reported in the literature.[2] Thermocatalysis is a widely known development through the years for chemical conversion of various hydrocarbons such as plastic solid waste.[3–8] Since the first report regarding methanol-involved hydrogen production in 1976, many efforts have been made to further improve activity.[9] Cu catalysts are commonly used at an industrial level for methanol steam reforming due to the low cost and the very high activity at relatively low temperatures (around 250 °C).[10] However, it is difficult to control the size and shape of these catalysts because of their high sensitivity to oxidation.[11] Moreover, they suffer from loss of specific surface area by sintering of their nanoparticles. To overcome these limitations, PdZn-based catalysts have been proposed. Even though they showed better selectivity towards hydrogen and better stability, their catalytic stability was lower than that of Cu catalysts. Although further improvements for PdZn-based catalysts enhanced their thermal stability, they still suffer from significant CO and CH_4 formation or coke formation.[12] Al_2O_3 and ZnO are often used as supports. The addition of ZrO_2 to Cu-based catalysts greatly enhances their activity and eliminates the production of CO.[13] The main reasons for the deactivation of catalysts during methanol steam reforming are catalyst poisoning and coking.[14] $CuZnGaO_x$ was applied for thermocatalytic methanol-involved hydrogen production *via* a non-syngas route and the methanol conversion reached nearly 100%.[15] Table S1 (ESI†) shows catalysts used for the methanol steam reforming reaction with reaction conditions and obtained results for H_2 yield, selectivity, and activity.

Cocatalysts play a crucial role in thermocatalytic methanol reforming, enhancing reaction efficiency and product safety by converting undesirable by-products. Notably, acidic or alkaline cocatalysts help transform unwanted compounds into more valuable or less hazardous substances. Despite the high activity and reduced CO formation reported with finely dispersed Cu-based catalysts, there is no consensus on the promotion mechanism.[16,17] Factors like the state of Cu, including its dispersion, valence, and stability, significantly influence catalytic performance and by-product selectivity. For instance, commercial $Cu/ZnO/Al_2O_3$ has achieved nearly 100% methanol conversion by manipulating the catalyst to specific nano-sizes.[18] Recent studies[19,20] also shed light on the *in situ* reduction process of Cu, from Cu^{2+} to Cu^0, highlighting both Cu^+ and Cu^0 as active sites that enhance catalytic activity. A similar phenomenon was observed in CeO_2 with changeable valence states.[21] Noble metals, known for their excellent thermal stability, prevent catalyst deactivation at high temperatures (>300 °C) but tend to drive thermocatalytic methanol conversion towards CO rather than CO_2,[22] which has been mitigated by introducing second promoters such as Zn, In, Cd, Au and Ga.[22,23]

Moreover, the choice of support can greatly affect activity and selectivity, as seen with Pd/ZrO_2 and Pd/ZnO catalysts, which respectively excel in hydrogen generation and CO_2 selectivity.[24] In another report, Au serves as an efficient cocatalyst in CeO_2 catalysed methanol-involved hydrogen production at low temperatures (<250 °C), where strongly bonded Au–O–Ce species were the main active species.[25] Recent developments in single-atom cocatalysts, like Pt and Ni atomically dispersed on α-molybdenum carbide (α-MoC),[26,27] demonstrate exceptional relatively low-temperature hydrogen production ($\leqslant 150$ °C), due to the synergistic action of single atoms and α-MoC. Similarly, single atom Pt_1 was deposited on CeO_2 to offer high hydrogen activity, which was 40 times higher than 2.5 nm Pt/CeO_2.[28] Recently, a lower temperature methanol-involved hydrogen production was reported,[29] where the synergy of Pt single atoms and Lewis pairs allowed porous CeO_2 to realise efficient H_2 generation at 120 °C with very low CO levels (0.027%). The optimal Pt_1/PN-CeO_2 catalysts exhibited a H_2 generation rate of 199 mol_{H_2} mol_{Pt}^{-1} h^{-1} at 135 °C.

The mechanism investigation for methanol steam reforming has been accomplished by many scientists not only for the most used Cu catalysts but also for various catalysts such as In_2O_3-, Cu/ZnO-, Ni–Cu-based and M-βMo_2C.[14,30–33] Surface species were found in methanol steam reforming systems.[34] Methanol preferred to adsorb at the top site with an O bond on the clean Cu(111) surface, with the possible pathways of methanol being CH_3O or CH_2OH.[35] The former was generated through direct dissociation due to lower activation energy and higher stability. The reaction mechanism of CeO_2 and Ni/CeO_2 showed that the preferable reaction process is described as $CH_3OH \rightarrow CH_3O \rightarrow CH_2O \rightarrow CH_2OOH \rightarrow CHOOH \rightarrow CHOO \rightarrow CO_2$.[35,36] DFT calculations to understand better the catalytic cycles releasing H_2 and CO_2[16,37] and steady-state isotopic transient kinetic analysis (SSITKA) to study the detailed process involving methoxyl and CO species adsorbed on the catalyst were also performed.[38]

Thermocatalysis known for its classical roots and high-temperature efficiency demands substantial energy input. Nevertheless, it provides a well-established and versatile method for hydrogen generation that can operate under various conditions without relying on external energy sources. It boasts high activity, making it suitable for industrial applications. However, the further decrease of energy demands and substantially reducing operating temperature/CO_2 emission are considered as key challenges. Additionally, the formation of by-products, such as CO, CH_4 and coke, is an inherent issue in thermocatalytic processes, leading to a loss of catalytic selectivity and a shortened catalyst lifespan. Maintaining active sites at elevated temperatures, especially for oxidation reactions involving methanol and reduction reactions involving protons over metal catalysts and metal oxide catalysts, proves to be exceptionally challenging.

3. Photocatalytic methanol-based hydrogen production

Photocatalysis, a promising alternative to thermocatalysis, uses photons instead of heat to drive chemical reactions under ambient conditions. As shown in Fig. 2(a), thermocatalytic methanol reforming follows an "uphill" thermodynamic pathway, requiring external heat to overcome the activation energy barrier. In contrast, photocatalysis excites the catalyst with photons, generating the energetic charge carriers that lower the barrier, enabling a "downhill" reaction pathway without external heating. This allows photocatalytic methanol reforming to occur at lower temperatures, offering a more energy-efficient and sustainable approach.

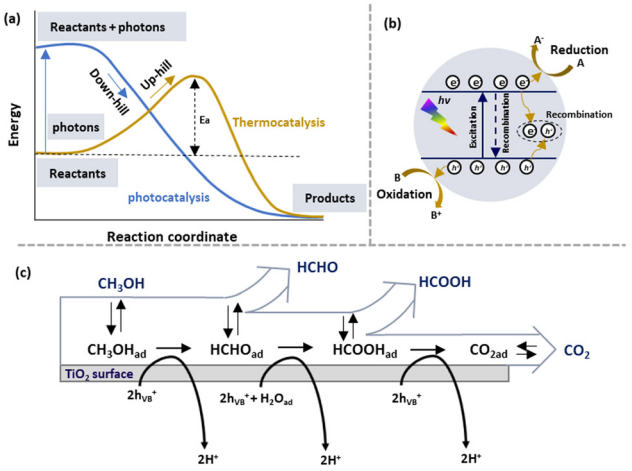

Fig. 2 (a) Difference in thermodynamics of photocatalysis and thermal catalysis. (b) Scheme for semiconductor photocatalysis. (c) The pathway for methanol oxidation on the TiO_2 surface.[39] (c) Reproduced from ref. 39 with permission from Elsevier, Copyright 2011.

3.1 Photocatalytic principles

Semiconductors have served as photocatalysts for water splitting since the 1970s, as they potentially presented favourable electronic properties,[40] UV and visible light absorption ability and advantageous charge transport kinetics. Unlike conductors, the semiconductors have a band structure.[41,42] The detailed fundamentals of photocatalysis have been widely discussed, as shown in Fig. 2(b).[42,43] Under illumination, photons with energy higher than or equal to the semiconductor band gap excite the electrons of the valence band (VB) into the conduction band (CB) and leave the corresponding holes in the VB. Then, these photogenerated charges reach the surface of the semiconductor due to the inbuilt potential followed by entering into the adsorbed molecules to drive reduction or oxidation reactions. Using highly sustainable solar energy, photocatalysis has been used in several research fields, including water splitting,[44–46] N_2 fixation,[47,48] degradation of organic pollutants,[49,50] CO_2 reduction,[51] *etc.* It is worth mentioning that the recombination of photogenerated electrons and holes is inevitable, resulting in reaction efficiency reduction.[52] Hence, it is essential to prevent the charge carrier recombination.

Since Fujishima and Honda reported water splitting to produce H_2 using the TiO_2 photoelectrode, significant attention has been paid to photocatalytic H_2 generation.[40] Methanol-based hydrogen production is less thermodynamically challenging for H_2 generation. The methanol conversion pathways can be illustrated using the following equations (eqn (1)–(4)).

$$CH_3OH \rightarrow HCHO + H_2 \quad \Delta G^0 = 64.1 \text{ kJ mol}^{-1} \quad (1)$$

$$HCHO + H_2O \rightarrow HCOOH + H_2 \quad \Delta G^0 = 47.8 \text{ kJ mol}^{-1} \quad (2)$$

$$HCOOH \rightarrow CO_2 + H_2 \quad \Delta G^0 = -95.8 \text{ kJ mol}^{-1} \quad (3)$$

Overall reaction:

$$CH_3OH + H_2O \rightarrow CO_2 + 3H_2 \quad \Delta G^0 = 16.1 \text{ kJ mol}^{-1} \quad (4)$$

3.2 Photocatalysts

Photocatalysts possessing a suitable band gap relative to the redox reactions are of intrinsic importance in photocatalysis, determining their light absorption range. In addition, the desired morphology engineering, long-term stability, and high surface area are favourable factors for activity enhancement. Many semiconductor materials have been employed as photocatalysts, including Cu_2O, NiO, MgO, $SrTiO_3$ *etc.*[53–59] Among them, TiO_2 is undoubtedly a widely studied semiconductor photocatalyst as it possesses favourable photochemical stability and is low cost. The first report of photocatalytic H_2 generation from methanol dates back to the 1980s.[60] Since then, several reports have shown H_2 production from methanol. For instance, reduced TiO_2 (black TiO_2) was used to enhance the methanol photo-reforming activity, where Ti(III) and defects were introduced in the anatase surface, exhibiting 10 mmol g^{-1} h^{-1} H_2 reaction rates with the assistance of Pt as a cocatalyst under simulated solar light irradiation.[61] Interestingly, a controlled study revealed that the H_2 production activity of Pt/black TiO_2 was limited at room temperature for methanol photo-conversion, which could be overcome by increasing reaction temperatures.[62] By controlling the crystalline phases of TiO_2, the H_2 evolution activity could be increased. For example, a mixed-phase of TiO_2 was achieved by controlling the annealing conditions and showed high photocatalytic H_2 production.[63,64] In another report, Pt/TiO_2 was optimised by tuning the anatase–rutile phase to obtain an extremely low CO concentration (<5 ppm) as a by-product. Due to the effective charge separation at the phase junction of two TiO_2 crystals, enhanced photocatalytic performance was observed, while CO production could be suppressed by adjusting the surface base.[65]

Representative photocatalysts without cocatalysts operated at room temperature shown in Table S2 (ESI†), including sulphides and nitrides, have also been used for methanol photo-reforming. Especially, CdS has received massive interest due to its strong visible-light response, though the poor photostability limits its application. This issue could be in part solved by the assistance of a supported cocatalyst. Also, annealing CdS under air could promote surface hydroxylation for alcohol dehydrogenation under visible light irradiation.[66] In 1982, Yanagida *et al.* observed H_2 evolution from a methanol–water mixture using ZnS.[67] Interestingly, $HOCH_2$–CH_2OH was the main oxidation by-product. Furthermore, they promoted the $HOCH_2$–CH_2OH selectivity to 52% in 1984, which was regarded as the first case for photocatalytic C–C coupling *via* free radical intermediates.[68] Moreover, the high selectivity of 95% towards $HOCH_2$–CH_2OH was achieved using colloidal ZnS and the primary intermediate was found to be a $^{\bullet}CH_2OH$ radical.[68] MoS_2 has been a relatively popular two-dimensional material in recent years for methanol-based hydrogen production.[69] The lamellar structure was conducive to the adsorption and desorption of reactants and by-products in catalytic reactions.[70] However, ordinary MoS_2 showed less marginal activity while defective MoS_2 was endowed with efficient H_2 evolution activity. Beyond inorganic metal oxide semiconductors, metal–organic frameworks (MOFs) have recently attracted much attention due to their semiconducting character.[71] Theoretically, the structure of MOFs allows them to be more versatile in photocatalyst design. A typical MOF UiO-66 (NH_2) was reported for H_2 generation from methanol photo-reforming thanks to efficient charge separation and prolonged charge lifetime.[72] Very recently, Ti-based MOFs were investigated to study the role of various ligands in methanol dehydrogenation. For instance, MIL-125 exhibited 38 times higher activity than NH_2-MIL-125 as holes in MIL-125 reacted with methanol, whereas holes in NH_2-MIL-125 were likely to be located on its N sites, which restricted methanol oxidation.[73] Followed by the catalyst exploration, covalent organic frameworks (COFs) were also used for photocatalytic water reforming of methanol, but they exhibited very limited H_2 yield.[74]

Overall, each type of catalyst presents unique strengths and limitations, requiring further improvement. Metal oxides like TiO_2 and ZnO are valued for their durability and cost-effectiveness, ideal for long-term applications. However, modifications such as doping and phase engineering are often necessary to improve visible light absorption and charge separation. Sulphides, including CdS and ZnS, offer excellent visible-light absorption but typically need strategies to ensure long-term stability due to susceptibility to photocorrosion. Polymers, especially C_3N_4, MOFs and COFs, provide a highly customisable platform with flexible structure that allows for readily tunable light absorption and active site configurations, though they face challenges of short lifetime of excitons and limited charge mobility.

In addition to the required band gap, it is more significant to reduce the reaction overpotential, which can be achieved by loading appropriate cocatalysts on the surface of a semiconductor. In detail, photogenerated electrons from the CB of the semiconductor flow to the Fermi level of cocatalysts until reaching an equilibrium.[75] This results in space charge accumulation in the semiconductor, leading to band bending to form the Schottky barrier at the interface if the cocatalyst work function is more positive than the semiconductor work function.[76] The Schottky barrier extracts the photogenerated electrons efficiently, thereby reducing the charge recombination. The following thus discusses a population of representative cocatalysts.

3.3 Cocatalysts

Similar to thermocatalysis, high-performing noble metals have been the most common cocatalysts used for photocatalytic conversion due to their positive Fermi levels, high redox potentials for electron extraction and small Schottky barrier.[77] The early discovery of photocatalytic H_2 generation from methanol-conversion dates back to the 1980s, in which Pd, Pt, and RuO_2 on TiO_2 were studied.[60] Among them, Pt/TiO_2

achieved a high quantum efficiency of up to 44%. Various metal cocatalysts have also been studied,[78] and the activity followed Pt > Au > Pd > Rh > Ag > Ru, due to the work function of noble metals for Schottky barrier construction. The cocatalyst's particle size has also been considered as one of the ways to increase the photocatalytic H_2 generation.[79] In a report, the Au/TiO_2 system was studied for H_2 production from methanol dehydrogenation, in which the H_2 production efficiency was inversely proportional to the particle size of the catalyst, suggesting that the smaller particle size could offer more active surface sites and high dispersion that were key to obtaining higher photocatalytic activity.[80] A detailed study on various noble metals on TiO_2 revealed that Pt was the most effective cocatalyst, followed by Au and Ag for photocatalytic H_2 evolution.[81] The obtained ESR results indicated that the Ti^{3+} concentration on Pt/TiO_2 was lower than Au/TiO_2, suggesting that the photogenerated electrons easily transferred from Ti^{3+} to Pt. These electrons reacted with the protons on Pt to produce H_2. The oxidation state of the metal cocatalysts was also reported to influence photocatalysis. For instance, a novel mesoporous CNT/TiO_2 hybrid photocatalyst, enhanced with Pt nanoparticles, achieved a high hydrogen generation rate of 40.6 mmol g^{-1} h^{-1}.[82] This efficiency arose from its unique structure: a network of interconnected TiO_2 nanocrystals provided abundant active sites and facilitated continuous charge transfer, while embedded CNTs created intimate interfaces that promoted charge separation, improved electron mobility, and reduced recombination. Additionally, oxygen vacancies formed during annealing introduced inter-bandgap states, lowering the flat band potential and enhancing charge transport. Oros-Ruiz *et al.* compared the performance of the metallic and oxidised Au as cocatalysts on TiO_2.[83] The metallic Au enhanced the activity significantly, whereas the oxidised Au showed an adverse effect as it acted as an electron sink. Similarly, in another report, metallic Pd-loaded ZnO was found to show higher activity at 200 °C compared to PdO loaded ZnO.[84] Interestingly, the reaction pathway of Pd-mediated methanol conversion was likely similar to Cu. First, CH_3OH was decomposed into HCHO followed by the formation of HCOOH, while HCHO reacted with H_2O and finally oxidised to CO_2 together with H_2 production. During this process, a small amount of CO production was inevitable. In addition to ZnO, Pd was also loaded on various substrates such as Al_2O_3, La_2O_3 and Nd_2O_3 and the expected activity was obtained, which again proved the role of Pd. Bowker *et al.* studied the contribution of the Pd loading amount on the photocatalyst surface and CH_3OH concentration for methanol-based hydrogen production.[85] Increasing the cocatalyst loading amount to 1% enhanced H_2 generation due to the increased interface between the metal and the semiconductor. In addition, atomic Pt assembled on TiO_2 (Pt_1/def-TiO_2) was reported to promote H_2 evolution, in which the Pt–O–Ti^{3+} surface formation was identified as an effective strategy.[86] This interface enhances charge transfer, achieving H_2 evolution rates of up to 52.7 mmol g^{-1} h^{-1}. The Pt–O–Ti^{3+} atomic interface facilitates the transfer of photo-generated electrons from Ti^{3+} defect sites to individual Pt atoms, thereby improving electron–hole pair separation. A summary of representative cocatalysts for methanol based H_2 production is also provided in Table S3 (ESI†).

Due to their low cost, earth-abundant transition metals have been applied in photocatalytic methanol conversion.[87] Among the various non-noble metals, Cu is an efficient cocatalyst due to its outer electron arrangement, being similar to Au and Ag. The work function of Au (5.1 eV) is greater than that of TiO_2 (4.4 eV), and electrons in the CB of TiO_2 overcome the energy barrier at the interface and migrate to the Au surface.[88,89] Similarly, the high work function (4.6 eV) of Cu compared to TiO_2 enabled it to extract the photogenerated electrons from the CB. In addition, its high electrical conductivity and plasmonic properties offered visible-driven methanol-based hydrogen production for H_2 generation.[90] Apart from the above basic advantages of Cu, altering the morphology of Cu also influenced the catalytic activity. For instance, Cu nanowires fabricated on TiO_2 nanorods were reported for H_2 production from methanol-based hydrogen production, in which Cu nanowires were obtained by a microwave-assisted thermal strategy. TiO_2 harvested the incident light and photogenerated the charge carriers that were successfully extracted by Cu before recombination.[91] In another report, Cu was incorporated into ultrafine TiO_2, resulting in extraordinary H_2 generation activity (2.88 mmol h^{-1} g^{-1}).[92] This enhancement was due to the efficient charge separation by Cu, active site engineering, and high surface area. However, the photocatalytic mechanism for the enhanced activity is still unclear due to the mixed states of Cu (Cu^{1+} and Cu^{2+}), especially the reversible process (Cu^{1+}/Cu^{2+}) during photocatalysis. The valency of Cu in the sample was identified to be between 0 and +1.[93] The high activity was attributed to the optimum valence caused by the oxidation and self-regulation of Cu. Furthermore, Cu^0 was highlighted as a potential alternative cocatalyst in H_2 generation from methanol based hydrogen generation, resulting in a remarkable increase of H_2 evolution (23 mmol h^{-1} g^{-1}) under UV irradiation.[94] An interfacial charge transfer mechanism in the Cu–TiO_2 system was proposed, according to which the Cu with multivalent states acted as active species for the photoreaction. In detail, Cu^{2+} acted as an electron trapping site for efficient charge transfer and was converted to Cu^+, in addition to working as the active site.[95] In a similar manner, a reversible copper activation was observed in a TiO_2 photocatalyst with single copper atoms (Cu/TiO_2), leading to a high hydrogen generation rate of 16.6 mmol g^{-1} h^{-1} and a significant quantum efficiency of 45% at 340 nm, thanks to its reversible and cooperative photoactivation process.[96] Our early work dramatically enhanced single atom Cu loading and dispersion on anatase by using MIL-125 as a precusor, leading to a hydrogen evolution rate of 101.7 mmol g^{-1} h^{-1} with the quantum efficiency of up to 56% at 365 nm.[97] *In situ* analysis identified Cu^{2+} as the active site for electron trap, which was then converted to Cu^+ to facilitate proton reduction to H_2. While very recent we found that the activity and stability of the photocatalyst could be remarkably improved by cooperating Pt nanodots with single atoms Cu, resulting in the hydrogen evolution rate of 476.8 mmol g^{-1} h^{-1} and the quantum efficiency of 99.2%.[98] This further enhancement is attributed to the synergy between the Cu single atoms and Pt nanodots, where the reversible Cu acts as an electron bridge between TiO_2 and Pt, thus accelerating proton reduction by Pt. Ni-based cocatalysts have received more attention after NiO was

used as a cocatalyst with $SrTiO_3$ for H_2 generation by the Domen group.[99] NiO_x could act as a dual-functional cocatalyst, where Ni extracted the photogenerated electrons and NiO captured the holes.[100] $Ni(OH)_2$ served a similar role to Ni in facilitating H_2 generation by the conversion of N^{2+}/Ni^0.[101–103] For example, $Ni(OH)_2$ quantum dots loaded on TiO_2 nanotubes exhibited a good H_2 evolution rate of 4.7 mmol g^{-1} h^{-1}.[103] The strong electronegativity enables $Ni(OH)_2$ to improve the shuttling of photogenerated charges, thus promoting H_2 evolution. The nanotubes, with a high surface area and unidirectional electron flow, mitigated charge recombination, while the $Ni(OH)_2$ cocatalyst promoted charge separation and electron transfer for efficient H_2 generation. In parallel, non-oxide cocatalysts such as Ni_2P have also attracted tremendous interest due to their graphite-like structure. For instance, Ni_2P-loaded TiO_2 exhibited an outstanding H_2 production rate of 9.38 mmol g^{-1} h^{-1} under a 300 W Xe lamp, which was 85 times higher than bare TiO_2.[104] The promoted charge separation was attributed to the upshifted Fermi level caused by the electron injection into Ni_2P. Another widely studied non-oxide cocatalyst is MoS_2. A high H_2 evolution was obtained by MoS_2 loaded TiO_2, which outperformed analogous Pt/TiO_2, Pd/TiO_2, and Ru/TiO_2. The decisive factor was the intimate contact between MoS_2 and TiO_2, thus promoting charge separation.[105] Additionally, loading MoS_2 onto the metal sulphide CdS also improved methanol photoconversion activity, resulting in a hydrogen production rate of 33.2 mmol g^{-1} h^{-1}—500 times higher than that of pristine MoS_2.[106] This improvement can be attributed to the interaction between MoS_2 as a cocatalyst and CdS as a photoharvester, which facilitates the efficient transport of photoexcited electrons.

Rare earth elements such as Gd^{3+} and Er^{3+} were also reported to enhance the H_2 evolution activity of $SrTiO_3$, primarily attributed to their up-conversion properties.[107,108] The inclusion of Er^{3+} in $SrTiO_3$ results in a notable increase in the H_2 formation rate, achieving up to 3.3 mmol g^{-1} h^{-1}, due to the up-conversion luminescence properties of Er^{3+}.[108] The incorporation of Er^{3+} leads to a redshift in the absorption edge and a modest improvement in visible light absorption.

Bimetallic cocatalysts have also been reported for H_2 evolution from methanol-based hydrogen production. Tunable NiPd bimetallic cocatalysts loaded on TiO_2 were reported for methanol based hydrogen generation.[109] Interestingly, Ni_1Pd_{10} with large aggregates (30 nm) loaded on TiO_2 indicated a higher H_2 formation rate (4.4 mmol g^{-1} h^{-1}) than that of $Ni_{10}Pd_1/TiO_2$ with a small cocatalyst size (3 nm). The bimetallic metals provided a synergistic effect contributing to charge transfer and acted as active sites for H_2 generation. Loading dual cocatalysts of Ni and Au onto TiO_2 resulted in an enhanced activity, yielding an impressive H_2 generation rate of 6.36 mmol g^{-1} h^{-1} in 50% methanol–water solution.[110] Similarly, PdAu bimetallic cocatalysts loaded on TiO_2 were reported to enhance the activity and the electronic structure. DFT was used to understand the role of dual cocatalysts[111,112] and it was found that the presence of Au suppressed *in situ* oxidation of Pd, allowing the oxidation ability of holes to be low enough to prevent methanol mineralisation. This way, PdAu promoted the formation of methyl formate, as opposed to CO_2, which was typically produced by PdO/TiO_2. In another report, the utilisation of Pt and Sn cocatalysts to modify TiO_2 was investigated, resulting in an H_2 evolution rate of 2 mmol g^{-1} h^{-1}.[113] The introduction of Sn was found not only to reduce the unfavourable OH groups and vacancies but also to assist higher Pt dispersion. Oxygen vacancies contributed to visible light absorption, while Sn introduction created electron trapping sites that improved charge separation and hydrogen production at lower tin contents. However, increased tin loading altered the Sn assemblies, affecting surface properties, acidity, and interfacial charge transfer, leading to diminished efficiency.

Apart from metal-based cocatalysts, nanostructured carbon materials including graphene oxide (GO), graphitic carbon nitride ($g\text{-}C_3N_4$) and carbon nanotubes (CNT) have also been reported as cocatalysts for methanol-based hydrogen production.[46,114,115] Graphene was reported to successfully extract the electrons from TiO_2, leading to a 41 times higher H_2 evolution rate than bare TiO_2.[116] Such a role was also observed in CNTs while depositing them on TiO_2.[53,114,117] The various synthesis methods of CNTs could influence the H_2 evolution. The catalysts obtained using the hydrothermal strategy were more efficient than those synthesised by photo-deposition or chemical reduction.[118] Depositing GO on the surface of the semiconductors could promote methanol based H_2 evolution by acting as an electron acceptor.[119,120] In addition, GO with an interlayer spacing of 0.42 nm served as an individual photocatalyst for H_2 evolution, and the activity in 20% methanol solution reached 2.8 mmol g^{-1} h^{-1}.[121] The removal of oxygen groups during photocatalysis reduces the bandgap and improves conductivity, while maintaining stable H_2 production.

Overall representative photocatalysts loaded with diverse cocatalysts for methanol based H_2 production are shown in Fig. 3. Noble metals like Pt and Rh remain the gold standard for methanol reforming due to their high stability, catalytic efficiency, and resistance to overoxidation. However, their high cost and the risk of CO byproduct formation, which can poison the catalyst, remain significant drawbacks. For instance, the photocatalyst $Rh/CaNb_6$ presented a quantum efficiency of up to 65% at 300 nm,[122] indicating its ability to efficiently facilitate charge separation and suppress recombination. In contrast, non-noble metals like Cu and Ni offer more economical alternatives with favourable electronic and plasmonic properties for visible-light absorption and charge transfer, though their quantum efficiency was generally below 20%.[102,105,106,123–125] In Cu systems, we found that the precise oxidation state control was crucial to mitigate deactivation and photocorrosion, with a single atom Cu system achieving a quantum efficiency of 56% at 365 nm.[97] A recent innovation combining Cu single atoms with Pt nanodots has reached a breakthrough quantum efficiency of 99.2% at 365 nm,[98] illustrating a promising strategy to enhance methanol reforming efficiency and selectivity by integrating the advantages of both single atoms and nanoparticles.

3.4 By-product selectivity to C1/C2

Compared with traditional thermal catalytic technology, the methanol conversion, apart from valuable H_2, into C1 or C2 by-products driven by photocatalysis is cleaner and more

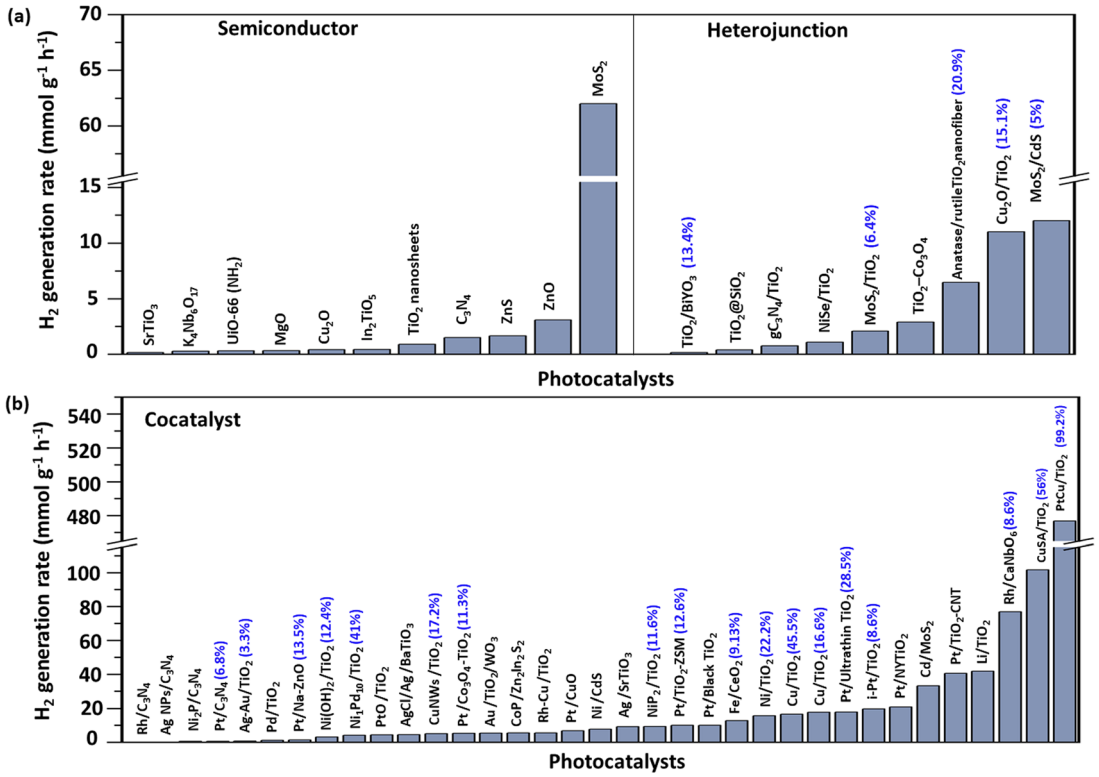

Fig. 3 Representative photocatalysts for methanol based H_2 production: (a) without cocatalysts or heterojunction structure and (b) loaded with different cocatalysts. The percentages highlighted in parentheses represent the quantum efficiency.

sustainable, making the catalytic reaction conditions milder. Most of the reports mainly deal with improving H_2 production and focus less on the valuable liquid by-products formed during the methanol oxidation reaction, while complete oxidation to CO_2 to maximise hydrogen production also results in carbon emissions, undermining the process sustainability. Furthermore, these oxygenates (*e.g.* formaldehyde, formic acid, and C_2 compounds) are much more expensive/valuable than either H_2 or CO_2 and the current industrial processes to produce these oxygenates are energy- and CO_2-intensive. Thus production of high-value organic by-products offers a more sustainable and economically viable alternative to the present industrial processes.

Formaldehyde (HCHO) and formic acid (HCOOH) are the two primary liquid intermediates produced from methanol photo-reforming and are more valuable than CO_x. For example, 37% HCHO and 98% HCOOH are three times more expensive than pure methanol. Typically, methanol reforming produces three main products: HCHO, HCOOH, and CO_2. Under irradiation, methoxy species derived from methanol are adsorbed onto the surface of metal oxides, leading to the subsequent formation of HCHO and HCOOH. In 1996, HCHO was detected from methanol photo-reformation using anatase TiO_2, demonstrating that the produced hydroxyl radicals oxidise the intermediate. Inspired by the initial finding, various types of TiO_2 were developed to explore the photo-formation pathways of HCHO from methanol. The process proved faster under inert conditions than in an O_2 atmosphere, with HCHO emerging as the sole oxidized by-product.[126] We found that PtCu–TiO_2 was highly efficient in catalysing the oxidation of methanol to HCHO, achieving a high selectivity of approximately 98.6% for HCHO. Subsequently, other non-noble metals such as Cu, Ni, and Co were loaded on anatase type TiO_2 to study the role of metals in the efficiency of methanol photo-reforming.[127] The primary products observed were HCHO and H_2, with a minor presence of HOOH. Excess photoexcited electrons migrated to metal sites, enhancing H^+ reduction and charge separation, while traces of Cu^{2+} suggested partial oxidation of Cu by photo-generated holes. Felipe *et al.* further investigated the influence of Au on TiO_2, focusing on by-product selectivity towards HCHO and HCOOH.[128] They found that increasing CH_3OH concentration boosted catalytic activity by 50%. This enhancement was attributed to the increased availability of reactants at the catalyst surface, facilitating the formation of key intermediates and promoting effective separation of photogenerated electron–hole pairs. Furthermore, higher light intensity improved the selectivity towards HCHO by 38% and HCOOH by 62%. At moderate light intensities, back reactions could overshadow hydrogen production. In contrast, higher intensities generated an excess of electrons that competed with back electron transfer and reduced side reactions, ultimately enhancing the production of hydrogen and intermediates.

When producing H_2, simultaneous photocatalytic C–C coupling of methanol to C_2 by-products like ethylene glycol ($HOCH_2CH_2OH$) is promising yet challenging, with limited reports citing success using metal sulphides such as ZnS and CdS. Initially, in 1982, H_2 was generated from methanol under

UV irradiation with low activity (0.17 mmol g^{-1} h^{-1}).[67] Subsequent studies using ZnS achieved a high selectivity for producing $HOCH_2CH_2OH$ from aqueous methanol, with the selectivity later enhanced to 52%, marking a significant advancement in photo-assisted C–C coupling through free radical intermediates.[32] Further investigations into colloidal ZnS increased the selectivity to 95% after 6 hours of irradiation, with characterisation studies indicating that the $^{\bullet}CH_2OH$ radical was the primary intermediate.[129,130] In another report, the porous MoS_2/CdS photocatalyst was explored for the conversion of CH_3OH to $HOCH_2CH_2OH$ through efficient activation of the C–H bond.[106] This process generated a hydroxymethyl radical ($^{\bullet}CH_2OH$), which readily desorbed from the catalyst surface to undergo coupling. The system achieved a quantum efficiency of 5% at 450 nm. Advanced characterization and computational analyses confirmed the reaction mechanism, which involved C–H bond scission followed by C–C coupling, competing with the activation of O–H bonds that led to aldehyde formation. Additionally, classic cocatalysts like Pd, Pt, MoS_2, and CoP were employed on $Zn_2In_2S_5$ for methanol photo-conversion, with CoP showing the highest activity, producing $HOCH_2CH_2OH$ at a rate of 5.5 mmol g^{-1} h^{-1}.[131]

Methyl formate ($HCOOCH_3$) is another common C_2 product forming *via* the C–C coupling of methanol. The early photo-assisted $HCOOCH_3$ formation was reported in 1985 using MoO_3/TiO_2 photocatalysts.[132] The process involved primary oxidation of adsorbed CH_3O(a) species, converting them into HCOO(a) on plain TiO_2, with $HCOOCH_3$ as the main by-product. Incorporating a surface molybdate monolayer significantly enhanced the selectivity, while suppressing secondary oxidation reactions. At lower molybdate loadings, $HCOOCH_3$ still dominated as the primary oxidation product. However, once the molybdate monolayer was fully developed, dimethoxymethane became the predominant product, exhibiting nearly 100% selectivity at low conversions. This change in selectivity underscores the kinetic differences between the TiO_2 surface and the molybdate monolayer, with the latter providing a more controlled reaction pathway. By 2010, a peak selectivity of 90% for $HCOOCH_3$ was achieved in gaseous methanol conversion at room temperature, though the conversion rate was only about 10%.[133] Fundamental studies using Fourier Transform Infrared Spectroscopy revealed that methanol adsorbed on TiO_2 as molecular and dissociated species, with subsequent oxidation to form HCHO intermediates that underwent dimerisation to $HCOOCH_3$. Elevated temperatures also affected the adsorption equilibrium of intermediates on the catalyst surface, decreasing their availability for selective coupling reactions. The photo-oxidation of methanol on preoxidised TiO_2(110) yields $HCOOCH_3$ through a two-step photochemical process.[134] Initially, methanol thermally dissociates into methoxy groups (CH_3O) and water. Upon UV light irradiation, methoxy undergoes photo-oxidation to produce HCHO, which further reacts with transient formyl species to form $HCOOCH_3$. Mass spectrometry and scanning tunnelling microscopy confirmed this mechanism, showing methyl formate formation only when both methoxy and HCHO were present on the surface. In parallel, oxygen adatoms healed surface defects and reduced charge recombination but were not directly involved in the reaction. Silver nanoparticles (Ag NPs) on TiO_2 (P25) and SiO_2 significantly enhanced photocatalytic methanol oxidation under UV light.[135] On TiO_2, Schottky barriers at the Ag–TiO_2 interface prolonged charge carrier lifetimes, promoting methoxy oxidation to intermediates that coupled to form $HCOOCH_3$. On SiO_2, the plasmonic resonance of Ag NPs induced localised electric fields, driving methanol oxidation through a distinct mechanism. Both systems outperformed their bare counterparts, with Ag/SiO_2 achieving a peak MF production rate of 23.46 mmol g^{-1} h^{-1}, highlighting the role of Ag NPs in improving selectivity and activity. Additionally, TiO_2-supported Cu catalysts facilitated methanol oxidation to $HCOOCH_3$ in the gas phase, achieving a $HCOOCH_3$ production rate of 56.4 mmol g^{-1} h^{-1}.[136] The ultra-small CuO improved the charge carrier transfer to promote activity. A similar mechanism of CuO was reported on CuZnAl and ZnO photocatalysts, showing a $HCOOCH_3$ selectivity of 50%.[137] Besides, ethanol production from methanol conversion was also reported using GaN, in which $^{\bullet}CH_2OH$ reacted with methanol to form ethanol.[138] Very recently, ethene production from two CH_3OH molecules was reported using surface engineered TiO_2,[139] with the high Ti^{3+} concentration facilitating methanol oxidation to HCHO and subsequent coupling to ethene, with HCHO as the main by-product and the remaining methanol reacting to produce ethene.

Table S4 (ESI†) provides a summary of the oxidized by-products and selectivity for various photocatalysts. Methanol conversion typically includes proton reduction to H_2, methanol oxidation, and C–C coupling. Enhancing photoexcited charge separation and the oxidation capacity of holes is crucial for achieving high activity. Reaction conditions such as pH, temperature, and reactant concentration significantly influence the adsorption of organic intermediates, thereby affecting by-product selectivity. Cocatalysts are pivotal in improving charge transfer, serving as active sites for activity enhancement and controlling oxidation processes. Additionally, the inclusion of suitable cocatalysts can alter surface affinity towards reactants or products, influencing the coupling pathway and the selectivity of the byproducts. Thus, the design of photocatalysts with a cocatalyst and the precise control of reaction conditions are vital for optimizing by-product selectivity. Various characterization techniques are essential to elucidate the mechanisms of C–H activation and C–C coupling. While some studies have shown successful conversion of methanol into valuable chemicals, they often come at the expense of reduced H_2 generation activity or selectivity. Therefore, developing efficient photocatalysts that maintain high selectivity while also ensuring favourable H_2 yields remains a significant challenge.

3.5 Process control

Several factors influence H_2 production from methanol reforming, including morphology, crystallinity, surface area, synthesis conditions and reaction atmosphere. Morphology and crystallinity of photocatalysts can be affected by the synthesis technology employed. Smaller photocatalysts typically facilitate

rapid transfer of photo-induced charge carriers to the material surface, decreasing recombination rates and increasing surface area, thus offering more reactive sites and boosting H_2 evolution. For instance, protonated g-C_3N_4, treated with HNO_3, showed improved hydrogen production due to structural exfoliation that created ultra-small pores enhancing charge transfer and surface area. Additionally, the calcination temperature of the catalyst significantly affects hydrogen production. An example is the Ni–TiO_2 catalyst, which exhibited a hydrogen production rate of 1.0 $mmol^{-1}\ g^{-1}\ h^{-1}$ when calcined at 550 °C, due to improved crystallinity and surface activation.[140] However, higher calcination temperatures (above 650 °C) were found to negatively impact the hydrogen production rate, dropping to 0.150 $mmol\ g^{-1}\ h^{-1}$, possibly due to detrimental changes in catalyst shape and particle size. This observation was further supported by a study, where an N-doped TiO_2 catalyst calcined at 450 °C displayed a higher hydrogen generation rate (4.4 $mmol^{-1}\ g^{-1}\ h^{-1}$) compared to the same catalyst calcined at 550 °C (3.8 $mmol^{-1}\ g^{-1}\ h^{-1}$), with performance deteriorating further at 650 °C (3.4 $mmol^{-1}\ g^{-1}\ h^{-1}$).[141] These findings suggest that elevated calcination temperatures increase the particle size, reducing the catalyst's dispersion and electron availability, which in turn affect its efficiency in hydrogen production.

While mild reaction temperatures mildly influence the thermodynamics of photocatalytic reactions, they significantly enhance the desorption of by-products from the catalyst surface, thus boosting photocatalytic activity. Huaxu *et al.* observed that increasing the reaction temperature from 45 °C to 55 °C led to a significant enhancement in the Pt/TiO_2 photocatalyst's H_2 generation rate, rising from 4.71 $mmol^{-1}\ g^{-1}$ to 15.18 $mmol^{-1}\ g^{-1}$ within 4 hours.[142] Similarly, Maggard noted optimal activity for a TiO_2 photocatalyst within the temperature range of 60–80 °C.[143] Conversely, lower temperatures tended to reduce H_2 generation activity, largely due to slower by-product desorption rates compared to reactant adsorption rates on the catalyst surface. Higher temperatures facilitated charge carrier transfer from the valence band to higher energy states, helping to prevent charge recombination. Velázquez *et al.*[144] used 2 wt% Pt on TiO_2 with bio-renewable oxygenated methanol to achieve 13 $mmol^{-1}\ g^{-1}\ h^{-1}$ at 20 °C, with increases to 19.5 $\mu mol^{-1}\ g^{-1}\ h^{-1}$ and 38 $mmol^{-1}\ g^{-1}\ h^{-1}$ at 40 °C and 60 °C, respectively, due to synergistic effects of light and thermal energy aiding electron excitation. Moreover, the pH of the methanol/water medium impacted photocatalytic H_2 production. Lin *et al.*[145] found a 2.25-fold activity increase for Pt–$TiO_{2-x}N_x$ as pH rose from 3 to 6.3, correlating to peak methanol adsorption at a pH matching the point of zero charge.[146] This condition maximised surface –OH groups essential for H_2 formation. Additionally, incident photon absorption crucially influences photocatalytic activity. Tambago *et al.* reported doubled hydrogen evolution activity with increased irradiation intensity from 33 mW cm^{-2} to 70 mW cm^{-2}.[147] This effect was confirmed by Baniasadi,[148] who saw a 20% increase in hydrogen generation activity by boosting light intensity from 900 W cm^{-2} to 1000 W cm^{-2}.

3.6 Mechanistic understanding

According to early mechanistic research on intermediates from photocatalytic methanol-involved hydrogen generation proposed by Kawai *et al.*,[60] methanol was progressively degraded on the TiO_2 surface to form HCHO, HCOOH, and finally CO_2, accompanied by H_2 production as the reduction product. Fig. 2(c) illustrates the pathway for methanol photooxidation on the TiO_2 surface,[39] highlighting stages of adsorption/desorption and chemical transformation. The multistep oxidation process introduces complexity due to the formation of liquid intermediates. Rapid production of HCHO with no detection of other liquid products suggested it as the initial step in methanol photo-reforming. Further studies on Pt/TiO_2 and Au/TiO_2 catalysts revealed a mechanism of $CH_3OH \rightarrow HCHO \rightarrow HCOOH \rightarrow H_2$ and CO_2, with Au's surface plasmon resonance enabling Au–Pt/TiO_2 to operate under visible light. However, CO and CH_4 were observed when switching from UV light to visible light irradiation, with CO adsorption deactivating active species on the semiconductor. Thus investigating surface species and photocatalytic charge mobility plays a pivotal role in advancing the understanding of photocatalytic processes. It helps unravel the complex surface chemistry involved, including adsorption, activation, and desorption processes, leading to improved catalyst performance and reaction kinetics. Transient absorption spectroscopy (TAS) is a reliable technique to investigate photophysics during methanol-based hydrogen production.[149] Recently, a unique electron-accepting photocatalyst, Cu single atom loaded TiO_2 (CuSA–TiO_2), was reported.[97] The transient absorption spectroscopy (TAS) spectra indicated the electron features, where modified TiO_2 exhibited a reduced electron signal after loading CuSA, suggesting that electrons were effectively trapped from TiO_2 to CuSA. When adding Ag^+ as an electron scavenger, a decreased signal of CuSA–TiO_2 was observed due to the consumption of electrons by Ag^+. As expected, CuSA–TiO_2 showed a similar profile of photoelectron decay to pure TiO_2, indicating the electron extraction by CuSA. Femtosecond TAS was also used to investigate the transportation dynamics of the twin Z-scheme catalyst CN/H–TiO_2.[150] Compared with CN and H–TiO_2, the TSP sample (Fig. 4(a)) exhibited the highest τ value, revealing the longest life of the carrier. Such a phenomenon was attributed to fast electron capture and slow optical carrier restructuring. In addition, *in situ* extended X-ray absorption fine structure (EXAFS) was used to investigate the density of orbital states involved in electron transitions, revealing the charge transfer pathway over PtCu–TiO_2 for methanol-based hydrogen production, as shown in Fig. 4(b).[98] By analysing Ti L-edge and O K-edge Extended X-ray Absorption Fine Structure (EXAFS) absorption features in the dark and during irradiation, the excitation of electrons from O 2p to Ti 3d under irradiation was observed. Cu was the most effective in abstracting electrons from TiO_2, followed by Pt as an electron-trapping site. The combination of Cu and Pt in PtCu–TiO_2 exhibited irreversible electron transfer characteristics. Furthermore, EXAFS can be used to reveal the electronic features of catalytic materials. For example, the k^2-weighted EXAFS spectra of MoS_2/CdS indicated an intensity reduction in Mo–Mo coordination, which was ascribed to the sheet-edges serving as H_2 production sites.[106] Jacquelin *et al.*[151] applied *in situ* electron paramagnetic resonance (EPR) spectroscopy to monitor electron transfer over

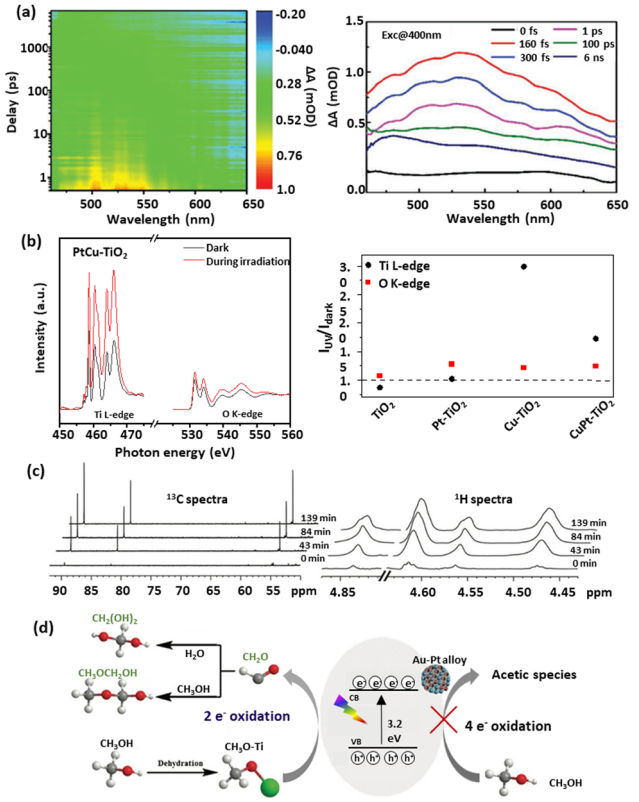

Fig. 4 Representative mechanism investigation *via* advanced techniques: (a) Transient absorption spectra of TSP.[150] (b) *In situ* Ti L-edge and O K-edge EXAFS spectra of PtCu–TiO_2 in the dark and during irradiation and the ratio of intensity under light irradiation to that under dark conditions.[98] (c) *In situ* NMR scheme of ^{13}C and ^{1}H over Au–Pt/TiO_2 for H_2 generation from selective methanol oxidation, and (d) the proposed mechanism[156] (a) Reproduced from ref. 150 with permission from John Wiley and Sons, Copyright 2023. (b) Reproduced from ref. 98 with permission from Springer Nature Limited, Copyright 2023. (c) and (d) Reproduced from ref. 156 with permission from Elsevier, Copyright 2023.

Au/TiO_2, revealing that different wavelengths of light stimulated the transfer through distinct electron excitation pathways within the Au particle. In another study of applying *in situ* EPR for charge mobility investigation, it was shown that pristine g-C_3N_4 favoured negative reduction potential, while pristine TiO_2 favoured positive oxidation potential.[150] In the case of the g-C_3N_4/H–TiO_2 heterojunction catalyst both oxidation and reduction abilities were significantly enhanced compared to pristine catalysts, confirming the spatial distribution of oxidation and reduction sites and the effective separation and transfer of photogenerated carriers through a twin Z-scheme charge transfer path. Time-resolved Raman and IR spectroscopy techniques have emerged as valuable tools in capturing ultrafast molecular transformations and charge transfer dynamics, essential for advancing the understanding of photocatalytic mechanisms. Time-resolved Raman spectroscopy, for instance, was effectively employed to explore photochemical processes on plasmonic metal nanoparticle surfaces. In a study conducted by Baumberg *et al.*,[152] metal nanoparticles generated energetic charges through nonradiative plasmon relaxation, enabling hot-electron-induced photoreduction reactions. By monitoring temporal changes in surface-enhanced Raman scattering signals from molecules adsorbed on Au nanoparticles, researchers observed real-time hot charge production, transport, and single-molecule redox events at plasmonic hotspots. Time-resolved IR absorption spectroscopy was used to monitor electron- and hole-capture reactions on TiO_2 and Pt/TiO_2 photocatalysts in the presence of dioxygen, water vapour, and methanol vapour. After a 355 nm UV pulse, a transient IR absorption band from 3000 to 1000 cm^{-1} appeared, attributed to photogenerated electrons in shallow mid-gap states.[153,154] Under vacuum, these electrons recombined with holes at a multi-exponential rate, while the presence of reactants altered electron decay rates, indicating reactant-driven capture reactions. This observation highlighted the influence of methanol on electron decay kinetics, advancing the understanding of reaction pathways in photocatalytic water-splitting. Expanding on this dynamic view, step-scan time-resolved FTIR spectroscopy provided a time-resolved approach to studying methanol oxidation on TiO_2 surfaces, indicating that long-lived electron decays correlated with photocatalytic activity.[155] This decay was linked to electron consumption for hydrogen production, facilitated by methanol or water adsorption on TiO_2. By examining proton transfer mechanisms, this approach offered mechanistic insights that enhanced those obtained from steady-state observations.

While time-resolved IR captures rapid transformations, *in situ* FTIR enables the identification of surface-bound intermediates throughout the reaction. Studies on Pt/TiO_2 during methanol photooxidation, for example, identified intermediates such as CH_2O(a), CH_2OO(a), and HCOO(a).[155] Furthermore, Haselmann *et al.*[157] developed a liquid-cell *in situ* attenuated total reflection (ATR)-FTIR setup, utilising top-irradiated ultraviolet light to investigate surface species of methanol-based hydrogen production over Pt/TiO_2. The FTIR spectra acquired during the photocatalytic reaction unveiled five noteworthy spectral components, including the following vibrations: (i) ν(O═H) bands, which originate from H_2O, methanol, and Ti–OH in TiO_2; (ii) ν(C–H) vibrations, derived from organic species; (iii) ν(C═O) signals, arising from gaseous and dissolved CO_2; (iv) bands of CO coordinated to Pt^0; and (v) ν(C═O) signals, stemming from carbonyl functionalities. To further explore the roles of free radicals and reaction intermediates, nuclear magnetic resonance (NMR) spectroscopy can be employed. For instance, the *in situ* NMR (^{13}C, ^{1}H) on an Au–Pt/TiO_2 system identified key methanol oxidation intermediates, with the ^{13}C NMR spectrum showing peaks at 55, 83, and 90 ppm corresponding to chemisorbed methoxy species, methanediol, and methoxymethanol, respectively.[156] As the reaction progressed (Fig. 4(c)), the increasing intensities of these peaks indicated the accumulation of methanediol and methoxymethanol, a trend corroborated by ^{1}H NMR spectra. This evidence supported a primary two-electron dissociation pathway in methanol oxidation in this work, leading to HCHO rather than a more complex four-electron route (Fig. 4(d)). In other words, methanol was initially adsorbed onto titanium hydroxyl (Ti–OH) sites, forming surface methoxy species

(CH_3–O–Ti), which were then oxidised by photogenerated holes or hydroxyl radicals ($^{\bullet}OH$) to produce HCHO. Due to its high reactivity, HCHO quickly reacted with water to form methanediol or with methanol to produce methoxymethanol on the Au–Pt/TiO_2 catalyst.

4. Integrating photocatalysis and thermocatalysis

With the above success, traditional photocatalysis still presents a low H_2 production rate and moderate selectivity for valuable by-products due to fast charge recombination and overoxidation. From a thermodynamic standpoint, methanol reforming is an endothermic reaction where heat is necessary. In parallel photochemical processes lower the activation energy barrier by facilitating the formation of key intermediates. Kinetically, according to the Arrhenius equation, the reaction activity increases with the temperature. Thus enhancements in photocatalytic performance *via* thermal effects should be favourable. Photo-thermo catalysis is divided into three categories: one involves photon energy to heating that is directly used to activate the reactants, another uses photon-induced surface plasma to drive the chemical reactions, and the last is to couple heating with photocatalysis (the concept of photon–phonon co-driven catalysis). The first two are widely reported and the last one is the most attractive fundamentally as it combines the advantages of the photocatalysis (high selectivity) and thermocatalysis (high activity).[158,159] Thus, the following focuses on the process of photon–phonon co-driven catalysis, which was firstly underlined by us about two years ago and we believe that it is the emerging and future research field to replace only photocatalysis, while distinguishing it from related concepts such as localized surface plasmon resonance (LSPR).

The photon–phonon co-driven catalytic process likely operates through a synergistic mechanism that enhances the efficiency and selectivity of chemical reactions. Photons generate electron–hole pairs, activating surface catalytic sites to drive redox reactions, while phonons may provide localised thermal energy to promote bond dissociation and improve intermediate hopping and product desorption dynamics. This interplay could create pathways that might be challenging to achieve with photon-driven or phonon-driven systems alone. The heating in this co-driven process can originate from two alternative sources: (i) heat induced by infrared light or (ii) externally supplied heating, which is dependent on the application environment. If the process takes place indoors, external heating is needed. If it takes place outdoors, IR from sunlight can provide heating energy.

A pre-heating is necessary for the vaporisation of methanol and water by the conventional gas phase reforming reaction.[160] The photo-thermo catalytic methanol reforming can potentially reduce the reaction temperature to as low as 100 °C. Nevertheless, lower conversion rates at lower temperatures and poor stability are some of the limitations of the early photothermal methanol reforming.[161] A solar-to-hydrogen production from methanol photothermal conversion achieved an efficiency of almost 33%, indicating the potential implementation of the synergistic effect of photocatalysis and thermocatalysis on the industrial methanol dehydrogenation.[162] It was later reported that the photo-thermocatalysis could dramatically enhance the H_2 production rates.[163,164] Photo-thermocatalytic materials are a complex of two different types of materials that ideally have to possess full-spectrum light harvesting ability, effective photo-to-thermal conversion, and abundant active sites. Some of the materials that can be utilised are the inorganic semiconductors, plasmonic metals, metal–organic framework catalysts and even polymers.

Domen's group has shown that raising reaction temperature from 25 °C to 58 °C increased the solar-to-hydrogen (STH) efficiency of the $SrTiO_3$:Al photocatalyst from 0.4% to 0.6%, as shown in Fig. 5(a).[165] Additionally, higher temperatures facilitated the generation of hydrogen through photocatalysis, whereas in most cases the temperature was within a lower range (from room temperature to up to 100 °C). This enhancement was attributed to the lower apparent activation energy (7.6 kJ mol^{-1}), reflecting the light-driven nature of the reaction, where electron–hole pairs drove redox processes. The observed reaction rates demonstrated stable hydrogen and oxygen evolution, with small gas bubbles released efficiently due to the thin water layer and hydrophilic panel design. This temperature dependence and sustained activity highlight the importance of optimising both catalyst performance and reactor design to maximise solar hydrogen production efficiency. CoO NPs were reported to show a significant increase in hydrogen production efficiency, ranging from 0.34 to 1.96 mmol h^{-1} g^{-1}, as the temperature was raised from 25 °C to 100 °C. Importantly, halting light irradiation ceased hydrogen generation, indicating the neglect of thermally induced hydrogen evolution.[166] A cost-effective NiO_x-enhanced TiO_2 catalyst was developed for hydrogen production from methanol dehydrogenation. Optimized with 5 wt% Ni, the catalyst produced hydrogen at 53.7 mmol h^{-1} g^{-1} under simulated AM1.5G sunlight at 260 °C, more than doubling the output without the light irradiation. Quantum efficiency measurements showed 66.24% at 380 nm, decreasing to 15.35% at 500 nm. In addition under visible light (>420 nm) at 260 °C, the yield increased dramatically to 26.9 mmol h^{-1} g^{-1} from 1.1 μmol h^{-1} g^{-1} at room temperature.[167] $CuInS_2$ offered a remarkable activity in photon–phonon co-driven conversion of methanol, with the hydrogen generation rate of 36 mmol g^{-1} h^{-1}. Its exceptional low-temperature H_2O molecule dissociation ability facilitated the formation of abundant interfacial OH radicals, thereby enhancing the C–H single bond breakage in methanol, reducing the apparent activation energy by 26%. Encouragingly, $CuInS_2$@MIL-101(Cr) demonstrated an excellent total turnover number (TON), reaching up to 16 775 within 65 hours of operation without any deactivation of the catalyst.[168] Recently, a nickel–iron bimetal catalyst supported by gallium nitride nanowires on a silicon substrate, NiFe/GaN, achieved a notable hydrogen evolution rate of 61.2 mmol h^{-1} g^{-1} from methanol–water under light illumination.[169] As the reaction temperature decreased from 90 °C to 10 °C, the hydrogen production rate dropped by a factor of four, and no hydrogen was detected when

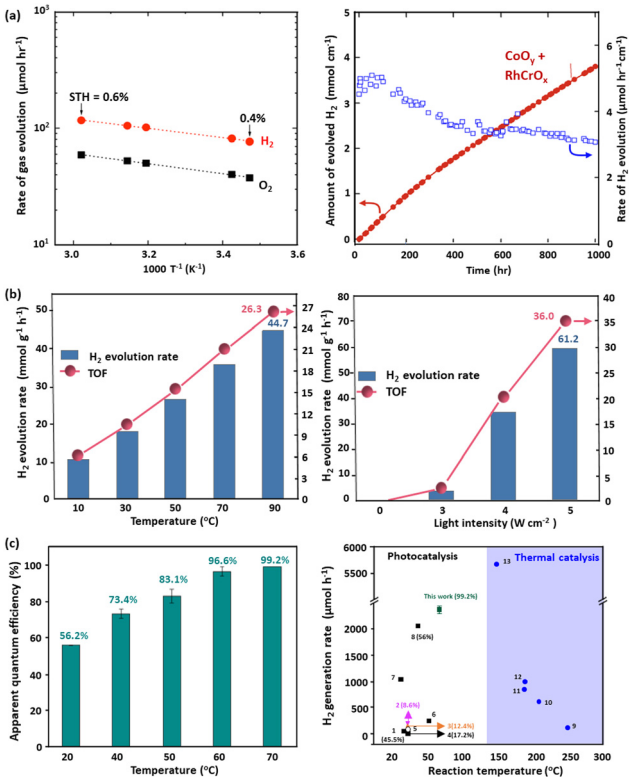

Fig. 5 (a) Temperature dependence of the water splitting activity and reaction time courses of $RhCrO_x/SrTiO_3$:Al under AM 1.5G simulated sunlight,[165] (b) photocatalytic effects of NiFe/GaN on chamber temperature and light intensity,[169] (c) The quantum efficiency of PtCu–TiO_2 at various temperatures and the activity comparison of diverse photocatalysts and thermal catalysts.[98] (a) Reproduced from ref. 165 with permission from Elsevier, copyright 2017. (b) Reproduced from ref. 169 with permission from the American Chemical Society, Copyright 2019. (c) Reproduced from ref. 98 with permission from Springer Nature Limited, Copyright 2023.

heating in the absence of light, highlighting the combined effects of photo- and thermal catalyses, as shown in Fig. 5(b). This result underscores the catalyst's ability to synchronise ultraviolet-driven charge carrier excitation with photothermal effects from visible and infrared light, maximising sunlight utilisation. The synergistic combination of Ni and Fe dramatically lowered the energy barrier of the potential-limiting step (*CHO → *CO), as confirmed by operando spectroscopy and density functional theory (DFT) calculations. The GaN NWs/Si platform enhanced light absorption, charge separation, and catalytic site dispersion while leveraging photothermal effects to further improve efficiency. The reaction pathway (*CH_3O → *CH_2O/*CHO → *CO → *CO_2) proceeded alongside water dissociation into reactive •OH species, enabling sustained hydrogen production. In a study that combined photocatalytic and thermocatalytic effects across the full solar spectrum to efficiently convert methanol into hydrogen, a CuZnAl-LDH precursor was used to fabricate a CuO/ZnO/Al_2O_3 nanocatalyst.[170] This catalyst demonstrated an impressive hydrogen production rate of 144.6 mmol g^{-1} h^{-1} at 130 °C, outperforming systems based solely on either photocatalysis or thermocatalysis. The most attractive was that the dual reaction sites of PtCu–TiO_2 exhibited extremely high hydrogen generation from a methanol/water mixture.[98] The catalyst's activity soared to 476.8 mmol g^{-1} h^{-1} when increasing the temperature from 25 °C to 70 °C, with no hydrogen observed in the absence of illumination, as shown in Fig. 5(c).[98] The synergistic approach leveraging both photons and phonons significantly enhanced the catalytic performance and efficiency in methanol reforming, which outperforms all photocatalysts and is comparable to the best thermal catalysts. Another example is a recent study that revealed photocatalytic hydrogen evolution boosted by the solar-heat, where SAAg-*g*-C_3N_4 demonstrated a good activity and stability.[171] The observed catalytic enhancement of SAAg-*g*-C_3N_4 was attributed to the favourable Gibbs free energy of the adsorbed hydrogen atom and the formed N–Ag bonds. When the temperature was elevated from 25 °C to 55 °C, the hydrogen generation rate significantly increased, underscoring the positive impact of solar heat on the photocatalytic process.

5. Reactor design

A meticulously engineered reactor can significantly enhance light absorption and mass transfer, thereby substantially increasing the yield and specificity of desired by-products. The design parameters of reactors, such as shape, size, thickness, and materials (*e.g.*, quartz and borosilicate), critically influence photocatalytic methanol-based hydrogen production.[172,173] The conventional packed bed reactor, often used in thermocatalysis for hydrogen production from methanol, is favoured industrially for its simpler design and construction, despite a high pressure drop across the reactor.[174,175] Recent studies, including extensive experimental and theoretical simulations like computational fluid dynamics (CFD), have been conducted.[27,30,34,35,176–178] For instance, Karim *et al.*[179] investigated how deviations from isothermality in a packed bed reactor affected methanol steam reforming rates using a commercial CuO/ZnO/Al_2O_3 catalyst. They identified heat transfer limitations within the reactor bed and implemented a reduction in reactor diameter to enhance heat transfer, achieving near-isothermal operation and higher apparent catalyst activity. Chougule and Sonde explored the effects of temperature, steam-to-carbon (S/C) ratio, and operating conditions on methanol conversion in a tubular packed bed reactor (Fig. 6(a)).[180] Their findings, based on both simulation and experimental data, indicated optimal hydrogen generation and methanol conversion at a temperature of 300 °C with an S/C ratio of 1.4. Comparatively, Karim *et al.* assessed a coated-wall reactor where the catalyst bed is affixed to the reactor wall, noting advantages such as lower pressure drop, improved mass and heat transfer, and minimal catalyst usage.[181,182] In contrast, packed bed reactors with internal diameters between 1 and 4.1 mm exhibited limited heat transfer and temperature gradients up to 40 K. Hafeez *et al.* conducted a simulation study comparing the performance of packed bed and coated wall microreactors using a CuO/ZnO/Al_2O_3-based catalyst (BASF F3-01), observing comparable performance at equivalent temperatures.[183] Their case studies included variables such as temperature, residence time, steam to methanol ratio, and catalyst coating thickness, revealing that larger catalyst pellet sizes led to

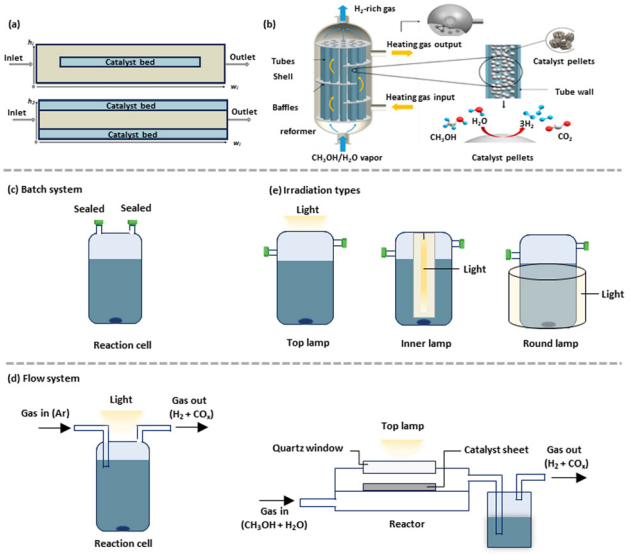

Fig. 6 Schematic representation of the reforming reactor: (a) packed bed and coated-wall packed bed microreactors, (b) a multi-tubular packed-bed reactor.[184] (c) Batch system and (d) flow systems. (e) The irradiation types. (b) Reproduced from ref. 184, no permission required.

internal mass transfer resistance and decreased methanol conversion. Additionally, thicker catalyst wall-coatings resulted in higher volumetric productivity for the same reactor diameter.[181] Another reactor type utilised for methanol-based hydrogen production is the multi-tubular packed-bed reformer, which also serves as a heat exchanger, shown in Fig. 6(b).[184] This reformer's structure includes baffles, tubes, and a shell, typically insulated to minimize heat loss. The tubes, filled with the $CuO/ZnO/Al_2O_3$ catalyst, were arranged in equilateral triangle bundles, supported by baffle plates that enhanced flow distribution and heat transfer efficiency between the tube and shell sides.

Inspired from the design of thermal catalytic reactors, photocatalytic reactors have evolved to include diverse configurations that enhance light utilization and catalytic efficiency. Batch reactors (Fig. 6(c)), a primary type, are often employed in the suspension systems. In the suspended systems, small catalyst particles are uniformly dispersed in solution. This configuration, widely used in batch reactors, enhances the external surface area exposed to irradiation and maintains a consistent temperature through uniform mixing, which improves the selectivity of desired products. However, suspended systems face challenges with mass transfer limitations between reactants and the catalyst surface, often restricting overall photocatalytic efficiency. Additionally, separating catalyst particles from the solution for recycling can be both costly and time-consuming. Flow reactors (Fig. 6(d)) present another configuration, where photocatalysts can either be suspended in an aqueous methanol solution or immobilized on substrates. These reactors often include a liquefaction section to capture intermediates produced during hydrogen generation from methanol. While the flow systems offer enhanced catalyst exposure, they may suffer from issues related to reactant accumulation and by-product formation, potentially impacting the selectivity and efficiency. In contrast, gas-phase reactors eliminate the need for catalyst separation, as the photocatalyst is immobilized on substrates *via* methods like suction or drop casting, simplifying recovery and enhancing sustainability. For example, Chiarello *et al.* reported that a flow reactor achieved 30% higher activity compared to a batch reactor due to enhanced mass transfer and photon utilization.[185] In these systems, a single oxidized product was typically produced in the gas phase, whereas more intermediates were found in the liquid phase. A similar gas phase system was reported over $Cu–TiO_2$ under ambient conditions,[186] where the H_2 generation activity from methanol-based hydrogen production was enhanced by a factor of 1.63 compared to that of the liquid phase counterpart. Such accessible activity was ascribed to promoted mass transfer and regulated reaction time when using a gas phase flow system.

Irradiation pathways are crucial for achieving uniform light distribution across the reactor and the catalytic surface, particularly when scaling up. As shown in Fig. 6(e), top irradiation is suitable for small systems, allowing light to penetrate directly through the catalyst bed. Inner irradiation, with the light source positioned inside the reactor, provides radial light distribution along the reactor, ensuring the relatively uniform activation of all catalyst particles. Round irradiation utilises light sources encircling the reactor, providing multidirectional exposure and is particularly advantageous in a heated reactor. In scaled-up systems, where light penetration is often limited to less than 1 mm in thicker catalyst beds, light guides or optical fibres are essential for directing light to specific photocatalytic sites, enhancing light harvesting.[187] Additionally, fixed-bed reactors can be scaled up by increasing the diameter while optimising light distribution, thus improving efficiency. Further improvements in flow reactors have been demonstrated by Goto *et al.*, who developed a panel-type reactor using Al-doped $SrTiO_3$, achieving a 10% solar hydrogen efficiency and scalable to at least one square metre.[188] The panels were angled at 10–20 degrees for optimal light capture, and a thin water layer facilitated consistent gas release while preventing pressure buildup. To further ensure efficient gas escape, the reactor's interior was hydrophilic, allowing stable gas bubble release. In both batch and flow reactors, advanced designs, such as fixed-bed setups with parabolic mirrors or solar concentrators, can further concentrate light onto the catalytic surface, boosting light intensity without extra energy input. Flow reactors also enable better control over methanol residence time, product desorption, and mass transfer. However, the limited reaction time on active sites in flow systems can sometimes reduce methanol conversion, requiring a balance between the residence time and the conversion efficiency.

Reactors for integrating thermocatalysis with photocatalysis have also been reported, thereby harnessing the synergistic effects of both methods to enhance reaction efficiency and output. One approach is to use a heating jacket if external heating is needed, allowing for uniform irradiation of the catalyst bed by an external heat source. Another approach involves direct photo-thermo systems, which minimize heat

transfer distances compared to traditional methods, resulting in faster start-up times and enhanced load flexibility.[189] Very recently, Erwin *et al.* developed a novel system integrating an aluminium-doped strontium titanate (Al:$SrTiO_3$) photocatalyst with a solar vapour generator.[190] This novel setup achieved highly efficient hydrogen generation through a dual mechanism that involved photocatalysis driven by UV-visible light and thermal energy from infrared (IR) light. This innovative design featured a floating photocatalyst layer above the solar vapor generator, ensuring that it only interacts with water vapor and not with liquid water. This strategic separation greatly enhanced the photocatalyst's longevity and effectiveness by protecting it from potential contaminants in natural water sources, thereby enhancing the hydrogen production process. The advancement of tandem reactors featuring high-performance catalysts is crucial for enhancing catalytic activity. Sun and Kim *et al.* developed a sophisticated dual-chamber microreactor incorporating metal-doped MOFs@COFs,[191] designed specifically for complex liquid–gas tandem reactions. This innovation highlighted the potential of advanced reactor designs in effectively handling intricate chemical processes. Moreover, progress in photo- and thermocatalysis notably enhances the catalyst efficiency and the specificity for activating chemical bonds. A prime example of this is the use of g-C_3N_4 nanosheets modified with AuCu alloy nanoparticles for the photothermal reduction of CO_2 to ethanol in a CEL-HPR reactor, which achieved a remarkable 93% selectivity. This high level of selectivity was achieved under photo-phonon synergistic conditions, with optimal ethanol production occurring at a reaction temperature of 120 °C. This underscored the benefits of incorporating precise thermal control in photocatalytic strategies.[188]

6. Challenges and perspectives

6.1 Developing catalysts with enhanced activity and selectivity

Exploring efficient photocatalysts is pivotal for advancing methanol-based hydrogen generation. Since the pioneering use of TiO_2 for photocatalytic hydrogen production in 1980, significant advances have been achieved, particularly at wavelengths $\leqslant$380 nm, nearing 100% quantum efficiency. Nonetheless, photocatalysts modified to absorb visible photons, *e.g.* up to 500 nm, despite enhancements like co-catalysts or vacancies, struggle to exceed 20% quantum efficiency. The main hurdles are rapid charge recombination and undesirable electron transfer pathways that compromise efficiency and selectivity.

Single-atom catalysts, especially those involving noble metals such as Pt and Pd, as well as non-noble metals like Cu, have demonstrated potential to boost methanol-based hydrogen production. Dual active site catalysts present a viable alternative to traditional noble metal catalysts by operating at lower temperatures and delivering higher hydrogen generation rates and stability. Future research should prioritize creating highly active photocatalysts that respond to both visible and infrared light. Modulating the selectivity of desired valuable products remains a challenging yet attractive goal. By adjusting the wavelength of incident light and carefully controlling the reaction pathways, the selectivity towards by-products can be significantly improved. Furthermore, the use of tandem catalysts can enhance by-product selectivity by enabling intermediates to be further converted into the desired products. Ensuring the structural integrity and long-term durability of these catalyst systems is essential for practical applications. Durability tests for methanol-based hydrogen generation typically span only tens of hours, and the in-depth deactivation analyses are scarce. Persistent challenges include the hundred- or thousand-hour stability and recyclability of catalysts.

6.2 Reactor design optimisation

Achieving high hydrogen production rates while maintaining operational stability necessitates precise reactor design. Batch reactors, although preferred for small-scale trials due to their precise control over experimental conditions, lack scalability and continuous operation capabilities. Conversely, flow reactors address these limitations by ensuring continuous reactant flow and enhanced mass transfer. Traditional reactors face significant challenges such as suboptimal light absorption due to the limited surface area or poor distribution of light in photocatalysis, high pressure drops and poor heat management. Recent advancements, including advanced microreactors and coated-wall reactors, even continuous stirred tank reactors (CSTR) begun to overcome these issues by improving mass and heat transfer, reducing pressure drops, and facilitating better temperature control for more efficient and rapid reactions. Additionally, advanced heat exchangers that recuperate and reuse thermal energy contribute to increased system efficiency. Innovative reactor configurations, such as spiral or honeycomb structures, can also optimize light distribution and thermal management.

6.3 Unravelling the underlying mechanisms

Identifying catalytic active sites and understanding reaction mechanisms are critical for future advancements in photocatalysis. Exploring the activity of C–H and O–H bond scission, as well as C–C coupling in various metals like Cu, Ni, Pd, Pt, and Ru, remains a significant area of interest. It is important to note that the deactivation mechanisms of catalysts under light exposure have been seldom explored; yet understanding these mechanisms could provide valuable insights for developing more effective and durable catalysts. Microkinetic modelling and quantitative structure–activity relationships will be crucial for designing more efficient catalysts.

Developing *in situ* detection methods is crucial for further understanding mechanisms. Techniques such as *in situ* infrared (IR) and Raman spectroscopy are effective for identifying and characterizing surface intermediates during catalytic reactions, aiding in the tracking of methanol's conversion to hydrogen. Techniques like time resolved transient absorption spectroscopy, *in situ* X-ray photoelectron spectroscopy (XPS) and extended X-ray absorption fine structure (EXAFS) offer more valuable insights into charge carrier dynamics and recombination processes, which should be extensively used in the emerging area.

6.4 Photon–phonon co-driven catalysis

Integrating photocatalysis with thermocatalysis utilizes the unique benefits of both systems. The energy from photons can be used to generate active charges, while thermal energy can aid in overcoming the small activation barriers of intermediate transformation and product desorption that limit the product selectivity. The photon–phonon co-driven process also intends to utilize the full solar spectrum for catalysis, *i.e.* IR photons to generate phonons for thermal catalysis and UV-visible photons for photocatalysis. As such the photon–phonon co-driven process would overcome the drawbacks of individual processes, enhancing the overall reaction kinetics. Thus the photon–phonon co-driven catalytic methanol reforming would dramatically decrease the temperature needed for the conventional thermal catalytic conversion, simultaneously maintaining a high selectivity for valuable products.

Integrating photons with other energies such as phonons, ultrasonic energy, microwave energy through a tandem system can also improve the selectivity of high-value liquid by-products. For example, an intermediate product is first generated through photocatalysis, and then phonon/ultrasonic energy is used to convert this intermediate into the desired liquid by-product. This approach requires a thorough understanding of the reaction mechanisms and the ability to control the reaction pathways to achieve high selectivity for the final product. Moreover, the integration of advanced characterization techniques to investigate the photothermal effect, elucidate detailed photon–phonon co-driven catalytic mechanisms, and precisely determine the distribution of various forms of energy conversion in the multi-energy-coupled catalysis will represent a critical area of research in the future.

6.5 AI promoted photon–phonon co-driven catalysis

Designing catalytic materials for photocatalytic methanol reforming presents numerous challenges due to the complex interactions that occur. This would be more complex in a photon–phonon co-driven process, such as surface chemical reactions, material restructuring, diverse energy coupling and so on. Integrating artificial intelligence (AI) into the design and optimisation process of these catalysts significantly enhances the accuracy and efficiency of screening potential catalyst materials. Advanced AI models, such as the sure independence screening and sparsifying operator, can identify key active sites that dictate catalyst performance in methanol reforming by analysing features such as the reducibility of active species and the adsorption strength of reaction intermediates and products. These models can predict catalyst selectivity for liquid products and emphasize the importance of the chemical properties of additive metals used as co-catalysts.

In addition to catalyst design, reactor optimisation is crucial for improving the efficiency of methanol reforming. Applying real-time monitoring technologies and computational modelling, including AI-based tools like COMSOL, facilitates dynamic adjustments to reactor conditions tailored to specific process requirements. This AI-driven approach, combined with experimental data, establishes a robust framework for optimising the photon–phonon co-driven catalytic process. It makes methanol reforming a more viable and economically attractive method for sustainable hydrogen production and the generation of valuable liquid byproducts. By leveraging the capabilities of AI, researchers can uncover patterns and relationships that might be overlooked using traditional methods, accelerating the discovery of high-performance catalysts, the exploration of the understanding of catalysis mechanisms and the selection of scalable reactors.

Data availability

No new data were generated or analysed in this study. The data underpinning the findings of this review are accessible through the original publications cited in the manuscript.

Conflicts of interest

There are no conflicts to declare.

Acknowledgements

All authors acknowledge the NSFC project (grant no: U23B20162 and 22250710677) and Beijing Municipal Project (C2022007). The project is also supported by Tsinghua University Initiative Scientific Research Program and UK EPSRC (EP/S018204/2).

References

1 X. K. Gu and W. X. Li, *J. Phys. Chem. C*, 2010, **114**, 21539–21547.
2 L. Li, W. Ouyang, Z. Zheng, K. Ye, Y. Guo, Y. Qin, Z. Wu, Z. Lin, T. Wang and S. Zhang, *Chin. J. Catal.*, 2022, **43**, 1258–1266.
3 S. M. Al-Salem, A. Antelava, A. Constantinou, G. Manos and A. Dutta, *J. Environ. Manage.*, 2017, **197**, 177–198.
4 S. M. Al-Salem, M. Van Haute, H. J. Karam, A. Hakeem, W. Meuldermans, J. Patel, S. Hafeez, G. Manos and A. Constantinou, *Ind. Eng. Chem. Res.*, 2022, **61**, 16383–16392.
5 A. Antelava, S. Damilos, S. Hafeez, G. Manos, S. M. Al-Salem, B. K. Sharma, K. Kohli and A. Constantinou, *Environ. Manage.*, 2019, **64**, 230–244.
6 A. Antelava, N. Jablonska, A. Constantinou, G. Manos, S. A. Salaudeen, A. Dutta and S. M. Al-Salem, *Energy Fuels*, 2021, **35**, 3558–3571.
7 S. Hafeez, E. Pallari, G. Manos and A. Constantinou, *Catalytic conversion and chemical recovery*, Elsevier Inc., 2019.
8 A. Antelava, E. Pallari, G. Manos and A. Constantinou, *Design and limitations in polymer cracking fluidized beds for energy recovery*, Elsevier Inc., 2019.
9 H. N. C. Kobayashi, *Chem. Lett.*, 1976, 1347–1350.

10 J. Zhao, R. Shi, Z. Li, C. Zhou and T. Zhang, *Nano Select*, 2020, **1**, 12–29.
11 X. He, Y. Wang, X. Zhang, M. Dong, G. Wang, B. Zhang, Y. Niu, S. Yao, X. He and H. Liu, *ACS Catal.*, 2019, **9**, 2213–2221.
12 J. L. C. Fajín and M. N. D. S. Cordeiro, *ACS Catal.*, 2022, **12**, 512–526.
13 A. A. Lytkina, N. A. Zhilyaeva, M. M. Ermilova, N. V. Orekhova and A. B. Yaroslavtsev, *Int. J. Hydrogen Energy*, 2015, **40**, 9677–9684.
14 M. V. Twigg and M. S. Spencer, *Top. Catal.*, 2003, **22**, 191–203.
15 K. M. K. Yu, W. Tong, A. West, K. Cheung, T. Li, G. Smith, Y. Guo and S. C. E. Tsang, *Nat. Commun.*, 2012, **3**, 1230.
16 N. Murakami, T. Chiyoya, T. Tsubota and T. Ohno, *Appl. Catal., A*, 2008, **348**, 148–152.
17 S. Neubert, D. Mitoraj, S. A. Shevlin, P. Pulisova, M. Heimann, Y. Du, G. K. L. Goh, M. Pacia, K. Kruczała, S. Turner, W. MacYk, Z. X. Guo, R. K. Hocking and R. Beranek, *J. Mater. Chem. A*, 2016, **4**, 3127–3138.
18 L. Pan and S. Wang, *Chem. Eng. J.*, 2005, **108**, 51–58.
19 H. Meng, Y. Yang, T. Shen, Z. Yin, L. Wang, W. Liu, P. Yin, Z. Ren, L. Zheng, J. Zhang, F. S. Xiao and M. Wei, *Nat. Commun.*, 2023, **14**, 7980.
20 D. Li, F. Xu, X. Tang, S. Dai, T. Pu, X. Liu, P. Tian, F. Xuan, Z. Xu, I. E. Wachs and M. Zhu, *Nat. Catal.*, 2022, **5**, 99–108.
21 J. Gao, J. Guo, D. Liang, Z. Hou, J. Fei and X. Zheng, *Int. J. Hydrogen Energy*, 2008, **33**, 5493–5500.
22 N. Takezawa and N. Iwasa, *Catal. Today*, 1997, **36**, 45–56.
23 X. K. Gu, B. Qiao, C. Q. Huang, W. C. Ding, K. Sun, E. Zhan, T. Zhang, J. Liu and W. X. Li, *ACS Catal.*, 2014, **4**, 3886–3890.
24 N. Iwasa, S. Kudo, H. Takahashi, S. Masuda and N. Takezawa, *Catal. Lett.*, 1993, **19**, 211–216.
25 B. W. L. Jang, R. Gläser, M. Dong and C. J. Liu, *Energy Environ. Sci.*, 2010, **3**, 253.
26 L. Lin, W. Zhou, R. Gao, S. Yao, X. Zhang, W. Xu, S. Zheng, Z. Jiang, Q. Yu, Y. W. Li, C. Shi, X. D. Wen and D. Ma, *Nature*, 2017, **544**, 80–83.
27 L. Lin, Q. Yu, M. Peng, A. Li, S. Yao, S. Tian, X. Liu, A. Li, Z. Jiang, R. Gao, X. Han, Y. W. Li, X. D. Wen, W. Zhou and D. Ma, *J. Am. Chem. Soc.*, 2021, **143**, 309–317.
28 L. N. Chen, K. P. Hou, Y. S. Liu, Z. Y. Qi, Q. Zheng, Y. H. Lu, J. Y. Chen, J. L. Chen, C. W. Pao, S. B. Wang, Y. Bin Li, S. H. Xie, F. D. Liu, D. Prendergast, L. E. Klebanoff, V. Stavila, M. D. Allendorf, J. Guo, L. S. Zheng, J. Su and G. A. Somorjai, *J. Am. Chem. Soc.*, 2019, **141**, 17995–17999.
29 S. Zhang, Y. Liu, M. Zhang, Y. Ma, J. Hu and Y. Qu, *Nat. Commun.*, 2022, **13**, 5527.
30 X. Tang, J. Li, Z. Fang, X. Dong, C. Sun, X. Qiao and X. Li, *Appl. Surf. Sci.*, 2022, **596**, 153635.
31 P. Tahay, Y. Khani, M. Jabari, F. Bahadoran and N. Safari, *Appl. Catal., A*, 2018, **554**, 44–53.
32 C. Mateos-Pedrero, C. Azenha, P. T. Pacheco, J. M. Sousa and A. Mendes, *Appl. Catal., B*, 2020, **277**, 119243.
33 V. Shanmugam, S. Neuberg, R. Zapf, H. Pennemann and G. Kolb, *Int. J. Hydrogen Energy*, 2020, **45**, 1658–1670.
34 S. T. Yong, C. W. Ooi, S. P. Chai and X. S. Wu, *Int. J. Hydrogen Energy*, 2013, **38**, 9541–9552.
35 Z. J. Zuo, L. Wang, P. De Han and W. Huang, *Int. J. Hydrogen Energy*, 2014, **39**, 1664–1679.
36 J. Reyna-Alvarado, O. A. López-Galán, M. Ramos, J. Rodríguez and R. Pérez-Hernández, *Catal. Today*, 2022, **392–393**, 146–153.
37 X. Yang, *ACS Catal.*, 2014, **4**, 1129–1133.
38 X. Wang, D. Li, Z. Gao, Y. Guo, H. Zhang and D. Ma, *J. Am. Chem. Soc.*, 2023, **145**, 905–918.
39 G. Luca, D. Ferri and E. Selli, *J. Catal.*, 2011, **280**, 168–177.
40 K. Fujishima and A. Honda, *Nature*, 1972, **238**, 37–38.
41 H. Kisch, *Angew. Chem., Int. Ed.*, 2013, **52**, 812–847.
42 A. L. Linsebigler, G. Lu and J. T. Yates, *Chem. Rev.*, 1995, **95**, 735–758.
43 A. J. Bard, *Science*, 1980, **207**, 139–144.
44 X. Li, J. Yu, J. Low, Y. Fang, J. Xiao and X. Chen, *J. Mater. Chem. A*, 2015, **3**, 2485–2534.
45 A. Kudo and Y. Miseki, *Chem. Soc. Rev.*, 2009, **38**, 253–278.
46 M. Thangamuthu, Q. Ruan, P. O. Ohemeng, B. Luo, D. Jing, R. Godin and J. Tang, *Chem. Rev.*, 2022, **122**, 11778–11829.
47 X. Chen, N. Li, Z. Kong, W. J. Ong and X. Zhao, *Mater. Horiz.*, 2018, **5**, 9–27.
48 H. Wang, X. Li, Q. Ruan and J. Tang, *Nanoscale*, 2020, **12**, 12329–12335.
49 D. S. Bhatkhande, V. G. Pangarkar and A. A. C. M. Beenackers, *J. Chem. Technol. Biotechnol.*, 2002, **77**, 102–116.
50 U. I. Gaya and A. H. Abdullah, *J. Photochem. Photobiol., C*, 2008, **9**, 1–12.
51 S. Xu and E. A. Carter, *Chem. Rev.*, 2019, **119**, 6631–6669.
52 A. Furube, T. Asahi, H. Masuhara, H. Yamashita and M. Anpo, *J. Phys. Chem. B*, 1999, **103**, 3120–3127.
53 K. Woan, G. Pyrgiotakis and W. Sigmund, *Adv. Mater.*, 2009, **21**, 2233–2239.
54 S. Kakuta and T. Abe, *ACS Appl. Mater. Interfaces*, 2009, **1**, 2707–2710.
55 Z. Liu, Z. Yin, C. Cox, M. Bosman, X. Qian, N. Li, H. Zhao, Y. Du, J. Li and D. G. Nocera, *Sci. Adv.*, 2016, **2**, e1501425.
56 A. Hameed and M. A. Gondal, *J. Mol. Catal. A: Chem.*, 2005, **233**, 35–41.
57 C. Jiang, K. Yip, C. M. A. Parlett, M. K. Bayazit, C. Ching, Q. Ruan, S. J. A. Moniz, A. F. Lee and J. Tang, *Appl. Catal., A*, 2016, **521**, 133–139.
58 A. Shoneye, J. Sen Chang, M. N. Chong and J. Tang, *Int. Mater. Rev.*, 2022, **67**, 47–64.
59 H. Wang, X. Yuan, H. Wang, X. Chen, Z. Wu, L. Jiang, W. Xiong and G. Zeng, *Appl. Catal., B*, 2016, **193**, 36–46.
60 T. Kawai and T. Sakata, *J. Chem. Soc., Chem. Commun.*, 1980, **764**, 694–695.
61 X. Chen, L. Liu and F. Huang, *Chem. Soc. Rev.*, 2015, **44**, 1861–1885.
62 B. Han and Y. H. Hu, *J. Phys. Chem. C*, 2015, **119**, 18927–18934.
63 C. H. Lin, J. H. Chao, C. H. Liu, J. C. Chang and F. C. Wang, *Langmuir*, 2008, **24**, 9907–9915.

64 J. Jitputti, Y. Suzuki and S. Yoshikawa, *Catal. Commun.*, 2008, **9**, 1265–1271.
65 Q. Xu, Y. Ma, J. Zhang, X. Wang, Z. Feng and C. Li, *J. Catal.*, 2011, **278**, 329–335.
66 Z. Jin, Q. Li, X. Zheng, C. Xi, C. Wang, H. Zhang, L. Feng, H. Wang, Z. Chen and Z. Jiang, *J. Photochem. Photobiol., A*, 1993, **71**, 85–96.
67 S. Yanagida, T. Azuma and H. Sakurai, *Chem. Lett.*, 1982, 1069–1070.
68 J. Wang, P. Yang, B. Cao, J. Zhao and Z. Zhu, *Appl. Surf. Sci.*, 2015, **325**, 86–90.
69 K. Chang, X. Hai, H. Pang, H. Zhang, L. Shi, G. Liu, H. Liu, G. Zhao, M. Li and J. Ye, *Adv. Mater.*, 2016, **28**, 10033–10041.
70 X. Huang, Z. Zeng and H. Zhang, *Chem. Soc. Rev.*, 2013, **42**, 1934–1946.
71 A. Corma and H. Garc, *J. Mater. Chem.*, 2010, **20**, 3141–3156.
72 C. G. Silva, I. Luz, F. X. Llabrøs and A. Corma, *Chem. – Eur. J.*, 2010, **16**, 11133–11138.
73 J. Wang, A. S. Cherevan, C. Hannecart, S. Naghdi, S. P. Nandan, T. Gupta and D. Eder, *Appl. Catal., B*, 2021, **283**, 119626.
74 Z. L. Wu, C. H. Wang, B. Zhao, J. Dong, F. Lu, W. H. Wang, W. C. Wang, G. J. Wu, J. Z. Cui and P. Cheng, *Angew. Chem., Int. Ed.*, 2016, **55**, 4938–4942.
75 M. R. Khan, T. W. Chuan, A. Yousuf, M. N. K. Chowdhury and C. K. Cheng, *Catal. Sci. Technol.*, 2015, **5**, 2522–2531.
76 X. Wang, G. Zhang, L. Yang, E. Sharman and J. Jiang, *Wiley Interdiscip. Rev.: Comput. Mol. Sci.*, 2018, **8**, 1–22.
77 J. Ran, J. Zhang, J. Yu, M. Jaroniec and S. Z. Qiao, *Chem. Soc. Rev.*, 2014, **43**, 7787–7812.
78 L. S. Al-Mazroai, M. Bowker, P. Davies, A. Dickinson, J. Greaves, D. James and L. Millard, *Catal. Today*, 2007, **122**, 46–50.
79 G. Wu, T. Chen, W. Su, G. Zhou, X. Zong, Z. Lei and C. Li, *Int. J. Hydrogen Energy*, 2008, **33**, 1243–1251.
80 G. L. Chiarello, M. H. Aguirre and E. Selli, *J. Catal.*, 2010, **273**, 182–190.
81 A. Naldoni, M. D'Arienzo, M. Altomare, M. Marelli, R. Scotti, F. Morazzoni, E. Selli and V. Dal Santo, *Appl. Catal., B*, 2013, **130–131**, 239–248.
82 A. Moya, A. Cherevan, S. Marchesan, P. Gebhardt, M. Prato, D. Eder and J. J. Vilatela, *Appl. Catal., B*, 2015, **179**, 574–582.
83 S. Oros-Ruiz, R. Zanella, R. López, A. Hernández-Gordillo and R. Gómez, *J. Hazard. Mater.*, 2013, **263**, 2–10.
84 N. Aas, T. J. Pringle and M. Bowker, *J. Chem. Soc., Faraday Trans.*, 1994, **90**, 1015.
85 A. Dickinson, D. James, N. Perkins, T. Cassidy and M. Bowker, *J. Mol. Catal. A: Chem.*, 1999, **146**, 211–221.
86 Y. Chen, S. Ji, W. Sun, Y. Lei, Q. Wang, A. Li, W. Chen, G. Zhou, Z. Zhang, Y. Wang, L. Zheng, Q. Zhang, L. Gu, X. Han and D. Wang, *Angew. Chem., Int. Ed.*, 2020, **59**, 1295–1301.
87 S. S. Yi, X. B. Zhang, B. R. Wulan, J. M. Yan and Q. Jiang, *Energy Environ. Sci.*, 2018, **11**, 3128–3156.
88 S. Kashiwaya, J. Morasch, V. Streibel, T. Toupance, W. Jaegermann and A. Klein, *Surfaces*, 2018, **1**, 73–89.
89 H. B. Michaelson, *J. Appl. Phys.*, 1977, **48**, 4729–4733.
90 M. Rycenga, C. M. Cobley, J. Zeng, W. Li, C. H. Moran, Q. Zhang, D. Qin and Y. Xia, *Chem. Rev.*, 2011, **111**, 3669–3712.
91 S. Xiao, P. Liu, W. Zhu, G. Li, D. Zhang and H. Li, *Nano Lett.*, 2015, **15**, 4853–4858.
92 Q. Liu, Q. Zhang, B. Liu and S. Li, *Chin. J. Catal.*, 2018, **39**, 542–548.
93 N. L. Wu and M. S. Lee, *Int. J. Hydrogen Energy*, 2004, **29**, 1601–1605.
94 W. T. Chen, Y. Dong, P. Yadav, R. D. Aughterson, D. Sun-Waterhouse and G. I. N. Waterhouse, *Appl. Catal., A*, 2020, **602**, 117703.
95 Y. Nosaka, S. Takahashi, H. Sakamoto and A. Y. Nosaka, *J. Phys. Chem. C*, 2011, **115**, 21283–21290.
96 B. H. Lee, S. Park, M. Kim, A. K. Sinha, S. C. Lee, E. Jung, W. J. Chang, K. S. Lee, J. H. Kim, S. P. Cho, H. Kim, K. T. Nam and T. Hyeon, *Nat. Mater.*, 2019, **18**, 620–626.
97 Y. Zhang, J. Zhao, H. Wang, B. Xiao, W. Zhang, X. Zhao, T. Lv, M. Thangamuthu, J. Zhang, Y. Guo, J. Ma, L. Lin, J. Tang, R. Huang and Q. Liu, *Nat. Commun.*, 2022, **13**, 58.
98 H. Wang, H. Qi, X. Sun, S. Jia, X. Li, T. J. Miao, L. Xiong, S. Wang, X. Zhang, X. Liu, A. Wang, T. Zhang, W. Huang and J. Tang, *Nat. Mater.*, 2023, **22**, 619–626.
99 I. Novotny and C. P. Bianchi, *Pflügers Arch. Eur. J. Physiol.*, 1973, **339**, 113–124.
100 M. A. Melo, S. A. Carminati, J. Bettini and A. F. Nogueira, *Sustain. Energy Fuels*, 2018, **2**, 958–967.
101 M. Hojamberdiev, M. Mansoob and Z. Kadirova, *Renewable Energy*, 2019, **138**, 434–444.
102 J. Yu, Y. Hai and B. Cheng, *J. Phys. Chem. C*, 2011, **115**, 4953–4958.
103 N. Lakshmana Reddy, K. K. Cheralathan, V. Durga Kumari, B. Neppolian and S. Muthukonda Venkatakrishnan, *ACS Sustainable Chem. Eng.*, 2018, **6**, 3754–3764.
104 Y. Chen and Z. Qin, *Catal. Sci. Technol.*, 2016, **6**, 8212–8221.
105 Y. J. Yuan, Z. J. Ye, H. W. Lu, B. Hu, Y. H. Li, D. Q. Chen, J. S. Zhong, Z. T. Yu and Z. G. Zou, *ACS Catal.*, 2016, **6**, 532–541.
106 S. Xie, Z. Shen, J. Deng, P. Guo, Q. Zhang, H. Zhang, C. Ma, Z. Jiang, J. Cheng, D. Deng and Y. Wang, *Nat. Commun.*, 2018, **9**, 1–7.
107 Y. Yang, L. Kang and H. Li, *Ceram. Int.*, 2019, **45**, 8017–8022.
108 D. Zhou, P. Zhai, G. Hu and J. Yang, *Chem. Phys. Lett.*, 2018, **711**, 77–80.
109 A. L. Luna, D. Dragoe, K. Wang, P. Beaunier, E. Kowalska, B. Ohtani, D. Bahena Uribe, M. A. Valenzuela, H. Remita and C. Colbeau-Justin, *J. Phys. Chem. C*, 2017, **121**, 14302–14311.
110 A. L. Luna, E. Novoseltceva, E. Louarn, P. Beaunier, E. Kowalska, B. Ohtani, M. A. Valenzuela, H. Remita and C. Colbeau-Justin, *Appl. Catal., B*, 2016, **191**, 18–28.

111 K. Czelej, K. Cwieka, J. C. Colmenares, K. J. Kurzydlowski and Y. J. Xu, *ACS Appl. Mater. Interfaces*, 2017, **9**, 31825–31833.
112 J. C. Colmenares, P. Lisowski, D. Łomot, O. Chernyayeva and D. Lisovytskiy, *ChemSusChem*, 2015, **8**, 1676–1685.
113 K. Majrik, E. Tálas, Z. Pászti, I. Sajó, J. Mihály, L. Korecz, E. Drotár and A. Tompos, *Appl. Catal., A*, 2013, **466**, 169–178.
114 C. G. Silva, M. J. Sampaio, R. R. N. Marques, L. A. Ferreira, P. B. Tavares, A. M. T. Silva and J. L. Faria, *Appl. Catal., B*, 2015, **178**, 82–90.
115 H. Wang, M. Thangamuthu, Z. Wu, J. Yang and H. Yuan, *Chem. Eng. J.*, 2022, **445**, 136790.
116 Q. Xiang, J. Yu and M. Jaroniec, *Nanoscale*, 2011, **3**, 3670–3678.
117 N. Naffati, M. J. Sampaio, E. S. Da Silva, M. F. Nsib, Y. Arfaoui, A. Houas, J. L. Faria and C. G. Silva, *Mater. Sci. Semicond. Process.*, 2020, **115**, 105098.
118 A. V. Puga, *Coord. Chem. Rev.*, 2016, **315**, 1–66.
119 H. El Marouazi, P. Jiménez-Calvo, E. Breniaux, C. Colbeau-Justin, I. Janowska and V. Keller, *ACS Sustainable Chem. Eng.*, 2021, **9**, 3633–3646.
120 S. Hu, J. Shi, B. Luo, C. Ai and D. Jing, *J. Colloid Interface Sci.*, 2022, **608**, 2058–2065.
121 T. Yeh, J. Syu, C. Cheng, T. Chang and H. Teng, *Adv. Funct. Mater.*, 2010, **20**, 2255–2262.
122 Y. Okamoto, S. Ida, J. Hyodo, H. Hagiwara and T. Ishihara, *J. Am. Chem. Soc.*, 2011, **133**, 18034–18037.
123 Z. Ding, H. Hu, J. Xu, P. Lin, C. Cui, D. Qian, P. Wang, L. Xu, J. Pan and C. Li, *Int. J. Hydrogen Energy*, 2018, **43**, 13190–13199.
124 J. Liu, G. Liu, M. Li, W. Shen, Z. Liu, J. Wang, J. Zhao, L. Jiang and Y. Song, *Energy Environ. Sci.*, 2010, **3**, 1503–1506.
125 S. Mansingh, D. K. Padhi and K. M. Parida, *Int. J. Hydrogen Energy*, 2016, **41**, 14133–14146.
126 C. Y. Wang, R. Pagel, D. W. Bahnemann and J. K. Dohrmann, *J. Phys. Chem. B*, 2004, **108**, 14082–14092.
127 K. Hirano, H. Asayama, A. Hoshino and H. Wakatsuki, *J. Photochem. Photobiol., A*, 1997, **110**, 307–311.
128 F. Varas-Concha, D. Guzmán, M. Isaacs and C. Sáez-Navarrete, *Energy Technol.*, 2018, **6**, 1871–1884.
129 S. Yanagida, T. Azuma, H. Kawakami, H. Kizumoto and H. Sakurai, *J. Chem. Soc., Chem. Commun.*, 1984, **325**, 21–22.
130 L. Chen, W. Gu, X. Zhu, F. Wang, Y. Song and J. Hu, *J. Photochem. Photobiol., A*, 1993, **74**, 85–89.
131 H. Zhang, S. Xie, J. Hu, X. Wu, Q. Zhang, J. Cheng and Y. Wang, *Chem. Commun.*, 2020, **56**, 1776–1779.
132 Y. C. Liu, G. L. Griffin, S. S. Chan and I. E. Wachs, *J. Catal.*, 1985, **94**, 108–119.
133 H. Kominami, H. Sugahara and K. Hashimoto, *Catal. Commun.*, 2010, **11**, 426–429.
134 K. R. Phillips, S. C. Jensen, M. Baron, S. C. Li and C. M. Friend, *J. Am. Chem. Soc.*, 2013, **135**, 574–577.
135 X. Yang, A. Zhang, G. Gao, D. Han, C. Han, J. Wang, H. Lu, J. Liu and M. Tong, *Catal. Commun.*, 2014, **43**, 192–196.
136 J. Liu, C. Han, X. Yang, G. Gao, Q. Shi, M. Tong, X. Liang and C. Li, *J. Catal.*, 2016, **333**, 162–170.
137 X. Liang, X. Yang, G. Gao, C. Li, Y. Li, W. Zhang, X. Chen, Y. Zhang, B. Zhang, Y. Lei and Q. Shi, *J. Catal.*, 2016, **339**, 68–76.
138 M. Liu, Y. Wang, M. Liu, Y. Wang, X. Kong, R. T. Rashid, S. Chu and C. Li, *Chem*, 2019, **5**, 858–867.
139 L. Mohrhusen, J. Kra and K. Al-shamery, *Phys. Chem. Chem. Phys.*, 2021, **2**, 12148–12157.
140 D. G. Calatayud, O. G. Díaz, A. C. Caballero and J. Ara, *Appl. Catal., B*, 2014, **153**, 192–201.
141 M. Taherinia, M. Nasiri and E. Abedini, *Environ. Dev. Sustain.*, 2019, **21**, 1963–1975.
142 L. Huaxu, W. Fuqiang, C. Ziming, H. Shengpeng, X. Bing, G. Xiangtao, L. bo, T. Jianyu, L. Xiangzheng, C. Ruiyang, L. Wen and L. Linhua, *Int. J. Hydrogen Energy*, 2017, **42**, 12133–12142.
143 Z. Zhang and P. A. Maggard, *J. Photochem. Photobiol., A*, 2007, **186**, 8–13.
144 J. J. Velázquez, R. Fernández-González, L. Díaz, E. Pulido Melián, V. D. Rodríguez and P. Núñez, *J. Alloys Compd.*, 2017, **721**, 405–410.
145 W. Lin, W. Yang, I. Huang, T. Wu and Z. Chung, *Energy Fuels*, 2009, **23**, 2192–2196.
146 M. Li, Y. Li, S. Peng, G. Lu and S. Li, *Front. Chem.*, 2009, **4**, 32–38.
147 H. M. G. Tambago and R. L. de Leon, *Int. J. Chem. Eng. Appl.*, 2015, **6**, 220–227.
148 E. Baniasadi, I. Dincer and G. F. Naterer, *Int. J. Hydrogen Energy*, 2013, **38**, 9158–9168.
149 J. Ma, T. J. Miao and J. Tang, *Chem. Soc. Rev.*, 2022, **51**, 5777–5794.
150 X. Ruan, C. Huang, H. Cheng, Z. Zhang, Y. Cui, Z. Li, T. Xie, K. Ba, H. Zhang, L. Zhang, X. Zhao, J. Leng, S. Jin, W. Zhang, W. Zheng, S. K. Ravi, Z. Jiang, X. Cui and J. Yu, *Adv. Mater.*, 2023, **35**, 1–9.
151 J. B. Priebe, M. Karnahl, H. Junge, M. Beller, D. Hollmann and A. Brückner, *Angew. Chem., Int. Ed.*, 2013, **52**, 11420–11424.
152 B. De Nijs, F. Benz, S. J. Barrow, D. O. Sigle, R. Chikkaraddy, A. Palma, C. Carnegie, M. Kamp, R. Sundararaman, P. Narang, O. A. Scherman and J. J. Baumberg, *Nat. Commun.*, 2017, **8**, 994.
153 A. Yamakata, T. A. Ishibashi and H. Onishi, *J. Mol. Catal. A: Chem.*, 2003, **199**, 85–94.
154 A. Yamakata, T. A. Ishibashi and H. Onishi, *Chem. Phys. Lett.*, 2001, **333**, 271–277.
155 T. Chen, Z. Feng, G. Wu, J. Shi, G. Ma, P. Ying and C. Li, *J. Phys. Chem. C*, 2007, **111**, 8005–8014.
156 F. Wang, Y. Jiang, D. J. Lawes, G. E. Ball, C. Zhou, Z. Liu and R. Amal, *ACS Catal.*, 2015, **5**, 3924–3931.
157 G. M. Haselmann, B. Baumgartner, J. Wang, K. Wieland, T. Gupta, C. Herzig, A. Limbeck, B. Lendl and D. Eder, *ACS Catal.*, 2020, **10**, 2964–2977.
158 C. Wang, Y. Xu, L. Xiong, X. Li, E. Chen, T. J. Miao, T. Zhang, Y. Lan and J. Tang, *Nat. Commun.*, 2024, **15**, 7535.

159 Y. Xu, C. Wang, X. Li, L. Xiong, T. Zhang, L. Zhang, Q. Zhang, L. Gu, Y. Lan and J. Tang, *Nat. Sustain.*, 2024, **7**, 1171–1181.
160 X. Yu, J. Zeng and Y. Xuan, *Energy Technol.*, 2019, **7**, 1–9.
161 Y. Pi, Z. Zengcai, W. Lin, B. Zhang and T. Wang, *AIChE J.*, 2023, **69**, 1–12.
162 X. Bai, D. Yuan, Y. Li, H. Song, Y. Lu, X. San, J. Lu, G. Fu, S. Wang and J. Ye, *iScience*, 2021, **24**, 102056.
163 X. Liu, L. Ye, Z. Ma, C. Han, L. Wang, Z. Jia, F. Su and H. Xie, *Catal. Commun.*, 2017, **102**, 13–16.
164 W. Chen, Y. X. Liu, X. Liang, S. Wang, X. Gao, Z. Zhang and Y. Fang, *J. Energy Storage*, 2022, **55**, 105405.
165 Y. Goto, T. Hisatomi, Q. Wang, T. Higashi, K. Ishikiriyama, T. Maeda, Y. Sakata, S. Okunaka, H. Tokudome, M. Katayama, S. Akiyama, H. Nishiyama, Y. Inoue, T. Takewaki, T. Setoyama, T. Minegishi, T. Takata, T. Yamada and K. Domen, *Joule*, 2018, **2**, 509–520.
166 S. Guo, X. Li, J. Li and B. Wei, *Nat. Commun.*, 2021, **12**, 1–10.
167 S. Fang, Z. Sun and Y. H. Hu, *ACS Catal.*, 2019, **9**, 5047–5056.
168 W. Lin, J. Li, Z. Zengcai, B. Zhang, X. Wu, Y. Pi and T. Wang, *Fuel*, 2024, **357**, 129990.
169 J. Li, B. Sheng, Y. Chen, J. Yang, T. Ma, C. You, Y. Li, T. Yu, J. Song, H. Pan, X. Wang and B. Zhou, *ACS Catal.*, 2023, **13**, 10153–10160.
170 X. Yu, L. Yang, Y. Xuan, X. L. Liu and K. Zhang, *Nano Energy*, 2021, **84**, 105953.
171 X. Li, S. Zhao, X. Duan, H. Zhang, S. Ze Yang, P. Zhang, S. P. Jiang, S. Liu, H. Sun and S. Wang, *Appl. Catal., B*, 2021, **283**, 119660.
172 A. G. Variar, M. S. Ramyashree, V. U. Ail, S. P. S, K. Sudhakar and M. Tahir, *J. Ind. Eng. Chem.*, 2021, **99**, 19–47.
173 C. McCullagh, N. Skillen, M. Adams and P. K. J. Robertson, *J. Chem. Technol. Biotechnol.*, 2011, **86**, 1002–1017.
174 J. Kang, Y. Song, T. Kim and S. Kim, *Int. J. Hydrogen Energy*, 2022, **47**, 3587–3610.
175 D. Iranshahi, A. Golrokh, E. Pourazadi, S. Saeidi and F. Gallucci, *Chem. Eng. Process.: Process Intensif.*, 2018, **132**, 16–24.
176 H. K. Huang, Y. K. Chih, W. H. Chen, C. Y. Hsu, K. J. Lin, H. P. Lin and C. H. Hsu, *Int. J. Hydrogen Energy*, 2022, **47**, 37542–37551.
177 J. Wang, H. Wang and P. Hu, *Sci. China: Chem.*, 2018, **61**, 336–343.
178 Z. J. Zuo, X. Y. Gao, P. De Han, S. Z. Liu and W. Huang, *J. Phys. Chem. C*, 2016, **120**, 27500–27508.
179 A. Karim, J. Bravo and A. Datye, *Appl. Catal., A*, 2005, **282**, 101–109.
180 A. Chougule and R. R. Sonde, *Int. J. Hydrogen Energy*, 2019, **44**, 29937–29945.
181 A. Karim, J. Bravo, D. Gorm, T. Conant and A. Datye, *Catal. Today*, 2005, **110**, 86–91.
182 P. Dokamaingam, S. Assabumrungrat, A. Soottitantawat, I. Sramala and N. Laosiripojana, *Int. J. Hydrogen Energy*, 2009, **34**, 410–421.
183 S. Hafeez, E. Aristodemou, G. Manos, S. M. Al-Salem and A. Constantinou, *RSC Adv.*, 2020, **10**, 41680–41692.
184 J. Zhu, S. S. Araya, X. Cui, S. L. Sahlin and S. K. Kær, *Energies*, 2020, **13**, 610.
185 G. L. Chiarello, L. Forni and E. Selli, *Catal. Today*, 2009, **144**, 69–74.
186 H. Jiao, J. Yang, X. Li, C. Wang and J. Tang, *Green Chem.*, 2022, **24**, 8345–8354.
187 P. Martínez Molina, K. W. Bossers, J. D. Wienk, J. Rohlfs, N. Meulendijks, M. A. Verheijen, P. Buskens and F. Sastre, *Chem. – Asian J.*, 2023, **18**, e202300405.
188 P. Li, L. Liu, W. An, H. Wang, H. Guo, Y. Liang and W. Cui, *Appl. Catal., B*, 2020, **266**, 118618.
189 M. Götz, J. Lefebvre, F. Mörs, A. McDaniel Koch, F. Graf, S. Bajohr, R. Reimert and T. Kolb, *Renewable Energy*, 2016, **85**, 1371–1390.
190 C. Pornrungroj, A. Bin Mohamad Annuar, Q. Wang, M. Rahaman, S. Bhattacharjee, V. Andrei and E. Reisner, *Nat. Water*, 2023, **1**, 952–960.
191 D. Sun, S. Jang, S. J. Yim, L. Ye and D. P. Kim, *Adv. Funct. Mater.*, 2018, **28**, 1–7.